

# UC Berkeley

## Research Reports

### Title

Fault Diagnosis and Safety Design of Automated Steering Controller and Electronic Control Unit (ECU) for Steering Actuator

### Permalink

<https://escholarship.org/uc/item/79w4589g>

### Authors

Tan, Han-Shue  
Bu, Fanping  
Koo, Shiang-Lung  
et al.

### Publication Date

2005-11-01

CALIFORNIA PATH PROGRAM  
INSTITUTE OF TRANSPORTATION STUDIES  
UNIVERSITY OF CALIFORNIA, BERKELEY

**Fault Diagnosis and Safety Design of Automated  
Steering Controller and Electronic Control Unit  
(ECU) for Steering Actuator**

**Han-Shue Tan, Fanping Bu,  
Shiang-Lung Koo Wei-Bin Zhang**

**California PATH Research Report  
UCB-ITS-PRR-2005-27**

This work was performed as part of the California PATH Program of the University of California, in cooperation with the State of California Business, Transportation, and Housing Agency, Department of Transportation, and the United States Department of Transportation, Federal Highway Administration.

The contents of this report reflect the views of the authors who are responsible for the facts and the accuracy of the data presented herein. The contents do not necessarily reflect the official views or policies of the State of California. This report does not constitute a standard, specification, or regulation.

Final Report for RTA 64A0028

November 2005

ISSN 1055-1425



# **Fault Diagnosis and Safety Design of Automated Steering Controller and Electronic Control Unit (ECU) for Steering Actuator**

## **Part I report for Development of Precision Docking Function for Bus Rapid Transit**

Han-Shue Tan, Fanping Bu, Shiang-Lung Koo and Wei-Bin Zhang

### **1. Introduction**

BRT has demonstrated its effectiveness to be a portion of the ‘backbone’ of an integrated transit network. It has become an effective means for attracting non-traditional transit riders and therefore can help to reduce urban transportation needs and traffic congestion. Many California transit agencies are planning to deploy BRT and have considered the use of dedicated lanes for BRT to be a very attractive option as it is less affected by automobile traffic and therefore can provide rail-like quality of service. In 1999, Caltrans generated a Caltrans Action Request (CAR) to request participation in the Bus Rapid Transit Project with VTA and other local transit providers. The future of BRT in California, as envisioned by Caltrans, would include a system of coordinated transit infrastructure, equipment, and operations that will give preference to buses on local urban transportation systems and the High Occupancy Vehicles (HOVs) lanes at congested corridors. The goal of the BRT service is to attract riders from single-occupancy vehicles, which could result in congestion relief without major infrastructure expansion. In the long-term, the proposed project may integrate the currently separate local transportation systems and transit services (offered by multiple transit agencies in a region) to provide express transit services enabled by interconnectivity between local systems and the State highway HOV system. Under the Caltrans Action Request, a BRT research program is established. One of the elements of this program is “Development of Precision Docking Function for Bus Rapid transit (named ‘Precision Docking’ or BPD from hereon)”.

Precision docking -- an innovative technology that enable bus to perform rail like level boarding has shown great potential for allowing fast boarding and alighting and therefore reducing the total trip time and improving service reliability and quality for BRT system. The bus precision docking seeks to achieve, with the help of electronic guidance technologies, a high docking accuracy and consistency that allows fast loading and unloading of passengers with special needs. In addition to the potential of serving as a major component of an advanced bus stop, such an automation capability would also reduce the skill and training requirements on the bus driver as well as the stress associated with achieving the high accuracy by the driver. In addition to precision docking, electronic guidance technologies also support a number of critical functions for BRT and transit applications. Once a bus is instrumented with electronic guidance, it can provide lane assist along dedicated BRT lanes. In the applications where dedicated lanes

are not available, lane assist can facilitate efficient operation at Queue Jump Lanes and can significantly benefit Bus Priority Systems. Electronic guidance can also support application at a bus depot where BPD technology can be useful as a component of the concept of Advanced Maintenance Station.

PATH has demonstrated precision docking function on automobiles. The objective of the BPD project is to develop and enhance the precision docking system for real-world bus operations. At the project early stage, Caltrans and PATH have decided to develop and demonstrate automated BRT using three automated buses (Demo 2003). Because of the synergy of these two programs, and due to the safety critical nature of precision docking/lane assist functions, PATH and Caltrans have determined to focus this project to safety designs of precision docking system. The two projects will complement each other and the mutual goal is to accelerate the deployment of precision docking/lane assist technologies.

This final reports the fault analysis of precision docking system and safety design of the safety critical elements for precision docking system. The report includes three Parts, including:

Part I provides a description of the Precision Docking System and reports analysis for fault diagnosis and safety design of automated steering controller and Electronic Control Unit (ECU) for steering actuator. It also reports a demonstration PATH conducted during the National Intelligent Vehicle Initiative demonstration organized by the US Department of Transportation Joint Program Office.

Part II report an analysis and design for a reliable direct drive for the steering wheel column of buses.

Part III reports power system reliability.

The report below is the Part I report: Fault diagnosis and safety design of automated steering controller and Electronic Control Unit (ECU) for steering actuator.

## **2. Description of Precision Docking System**

Bus docking system provides a special function under lane-assist Bus control systems. The system employs almost identical vehicle components for the general lane assist capabilities. In the software areas, except for the certain “docking” control algorithm specifics and the “docking” accuracy requirements, those of the precision docking system may not be too much different from those for the lane-assist control system. A typical bus docking system includes the following basic elements and functions:

- Lateral guidance system  
In principle, any lateral guidance technologies (such as GPS, DGPS/INS, machine vision, electronic marker system, magnetic tape, magnetic markers, transponders, etc.) can be a candidate for precision docking as long as it

satisfies the reliability and accuracy requirements for the specific precision docking application. Magnetic guidance system is chosen for this study because of its high reliability under almost all operational scenarios as well as providing accuracy to within a centimeter. A typical lateral guidance system may involve infrastructure support, sensors, signal processing and validation.

- **Steering actuator system**

The steering actuator system for an automated steering control vehicle can be any actuator that can change or modify the steering mechanism so that the “steer wheel” follows precisely the desired “steering command”. The power component can be hydraulic mechanical or electrical. It can be directly installed as a primary steering mechanism or it can be an add-on device that drives through the existing steering assist system. However, the requirements for the steering actuator do depend on the above system design configurations. Furthermore, higher speed operations often demand higher bandwidth while low speed requires more power. A decouple-able stand-alone intelligent servo control system is a preferred steering actuator configuration. In such framework, the actuator can then be treated as a “component” for the precision docking system and help to reduce the overall design complexity.
- **Lane-keeping and transition control system**

Lane-keeping and automatic/manual transition controls are the heart of the precision docking control system. It fulfills the design requirements and takes into account the following factors: steering actuator and mechanism, sensor accuracy and imperfections, various speeds and road geometry, fault detection and signal processing, driver intension and intervention, vehicle dynamics and environmental uncertainties, high speed bandwidth and low speed non-linearity. The design of robust and extremely reliable steering control and transition systems are key tasks for the precision docking system.
- **Driver vehicle interface (DVI) system**

Since precision docking system application requires smooth interfacing with drivers. A suitable interface between the automated control system and driver is essential. The interface system can be either complicated or simple. A complicated transition may require the driver to either follow certain strict operational procedures or observe certain transitional rules before transition. A simple, transparent but effective interface with the driver is almost always a better choice. However, a simple DVI often require rather complicated transitional software to smooth out all uncertainties both in the control system and from the driver.
- **Fault detection and management system**

The fault detection and failure management systems are the crucial components in any automated vehicle systems. It’s complexity increases as the complexity of the system increases. In the precision docking system designed under this project, all component failures are included in the design, although the design itself may not be comprehensive due to the limited resource and time.
- **Associated longitudinal control and sensing system (if applicable)**

The longitudinal control is generally not required in a precision docking system. However it can help the bus to stop smoothly at any predestinated location with high accuracy. Therefore an associated longitudinal control system will be a good optional control system that supports the precision docking operation.

One cautionary note: Any possible single point failure should have redundancy to protect the system safety and integrity. However such safety critical operational design is not implemented for this test system due to the resource limitation as well as the fact that it's design purpose is for studies and not for field operational tests.

Figure 2.1.1 depicts the major components for the PATH Precision Docking System using magnetic markers lateral guidance system. As seen in this figure, the major components are: front and rear magnetometers as the main lateral sensors, yaw gyro and speed as auxiliary sensors, add-on DC motor on the steering column as the steering actuator, computer with all the signal processing, control algorithms, and DVI controls as the intelligent center of the system, and button and switches, driver indicators, sound, passenger display and indicators as the DVI systems.

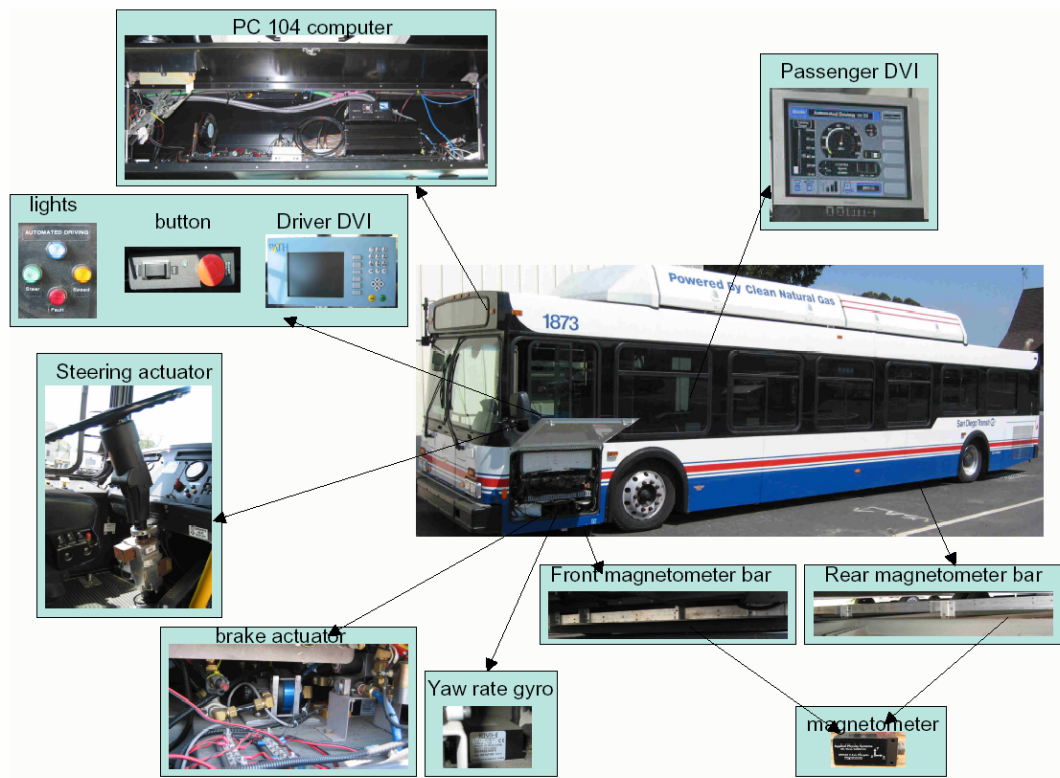


Figure 2.1.1 PATH Precision Docking System Components Diagram

Figure 2.1.2 illustrates the system block diagram of the PATH Precision Docking system. It includes hardware, software with various functions. The hardware consists of various switches, steering DC motor, vehicle sensors, computer, displays and audible units. The software consists of various software drivers, steering actuator algorithm, lateral control

algorithms, and DVI controls. The steering actuator control algorithm provides functions such as self-calibration, tight position servo, various mode transition and fault detection. The lateral control algorithms include lane-tracking control, transition control, trajectory planning, mode switching and failure detection and fault mode control. The DVI control tracks the control states, driver reactions, and provide appropriate interface for manual, automated, and transition controls. It also includes warning and emergency supports.

Figure 2.1.3 shows the software architecture of the PATH Precision Docking system. The core of the software architecture is a “public” subscribed database (db\_slv). All input/output drivers provide and interface with the database. All application software made its decision based on the real-time database information. The lateral control consists of the following blocks: vehicle I/O (sensor inputs), lateral control (sensor signal processing and various lateral controls), docking longitudinal control (algorithm interfacing with the longitudinal hardware for precise stopping), docking coordination, (coordinate longitudinal and lateral controls), steering actuator (steering hardware drivers), steering inner loop (steering servo and its associated intelligence), DVI inputs and outputs.

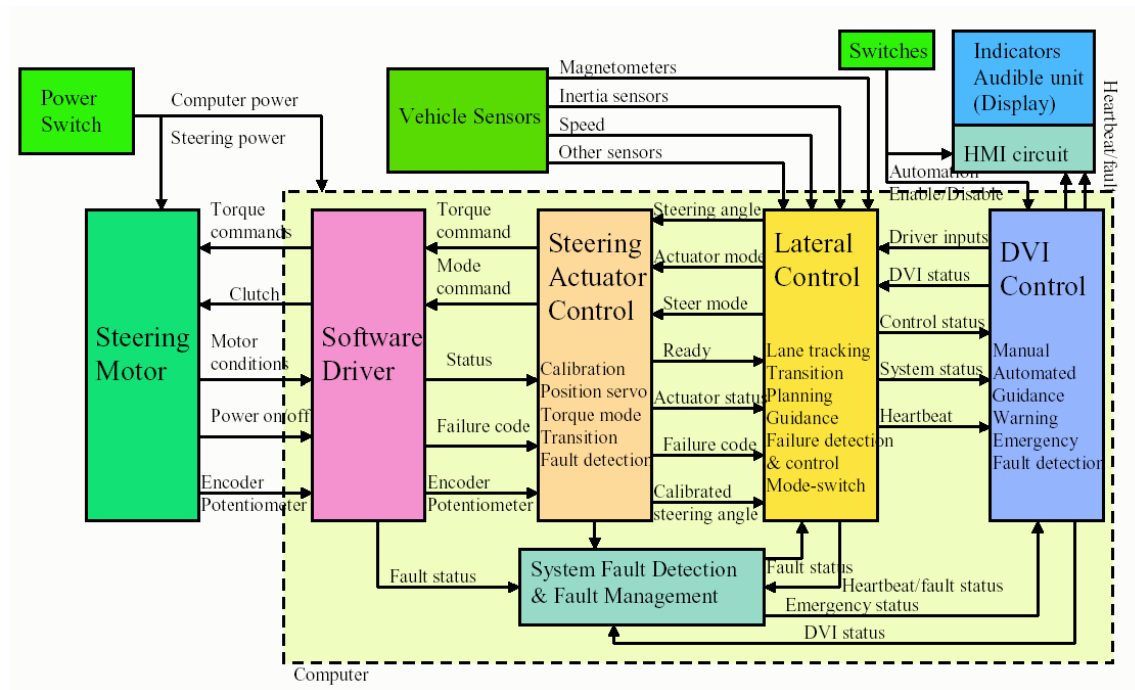


Figure 2.1.2 PATH Precision Docking System Block Diagram



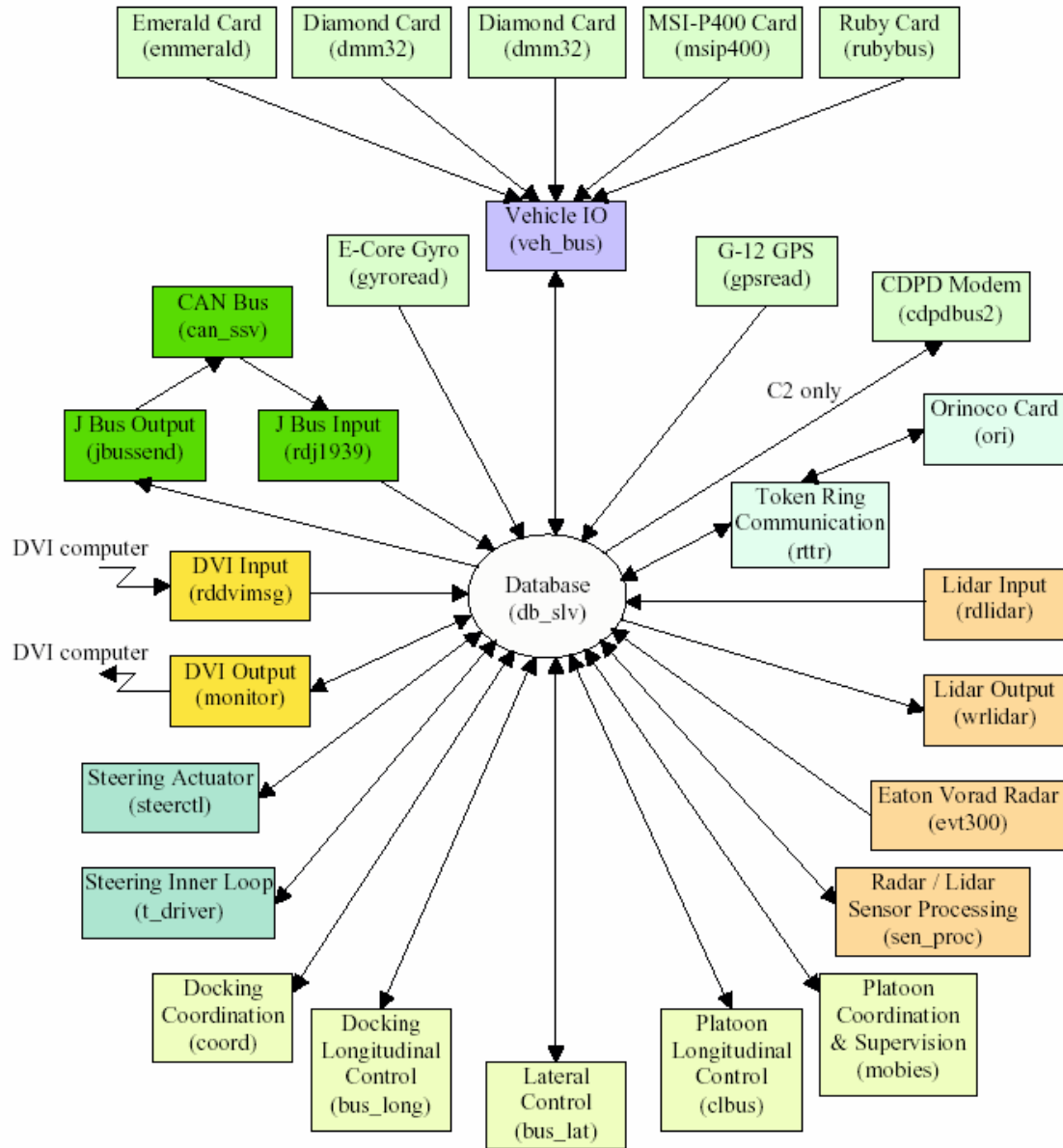


Figure 2.1.3 PATH Precision Docking Software Architecture

## 2.2 Development of the bus docking system

The tasks involved in the development of the bus docking system are listed as follows:

- System Design
  - Define and tradeoff performance requirements
  - Flow down component requirements from system performance requirements
  - Define and design system configuration
- Hardware and Software Development
  - Install magnetometer and design and verify signal processing for lateral sensing accuracy and reliability

- Install steering actuator and develop hardware driver
- Install yaw rate gyro
- Integrate longitudinal sensor, Jbus, and controls
- Analysis
  - Develop appropriate bus vehicle models
  - Predict system performance and evaluation
  - Develop driver model and characteristics for transition
- Control Algorithm Development
  - Design steering actuator servo control to account for various uncertainties and non-linearity; design appropriate component-level intelligence to relieve lateral control complexity
  - Design high performance lateral lane-tracking controller
  - Design high reliable transition control with on-demand capability
  - Design DVI control interface that support “transparent” driver/automated system transitions
- Safety Design
  - Design and evaluate the robustness properties for the system operations
  - Design failure detection for all sub-systems
  - Develop failure mode control
  - Evaluation possible redundancy and their effects and limitations

The basic precision docking system design involves four major development areas: lateral sensing system, steering actuator, control algorithms, DVI design and failure mode control. Subsections 2.3, 2.4, 2.5 and 2.6 will focus on the lateral sensing system, steering actuator inner loop control design and precision docking controller design. DVI and failure mode will be discussed in the Section 3.

## **2.3 Magnetic Marker Lateral Sensing System**

### **2.3.1 Introduction**

The development of a reliable and accurate lateral referencing system is crucial to the success of the lateral guidance system for precision docking. For the Automated Precision docking system, the accuracy requirement for the lateral sensing system is directly proportional to the required docking accuracy especially along the docking platform. The lateral sensing accuracy requirement was set to be better than 1 centimeter for the docking accuracy targeted to be better than the same value. The assumption is that the installation and measurement accuracy are randomly and evenly distributed along the correct position.

PATH has proposed and developed a lateral referencing and sensing system that is based on the magnetic markers embedded in the road center to provide the lateral position and road geometric information. The Bus steering guidance system based on such technology provides the control system with the following two fundamental pieces of information: the vehicle position with respect to the roadway, and the current and future road

geometry. Two arrays of magnetometers, one located behind the front bumper and the other at about 5 meters behind the front sensors, were used to “simultaneously” obtain front and rear lateral offset measurements.

Extensive development and experiments have been performed on magnetic marker-based lateral sensing systems for many PATH vehicles equipped with automated steering control. The vast knowledge available about this lateral sensing technique was one of the primary reasons that this technology was first chosen to support the Precision Docking steering guidance system. Other positive characteristics of this lateral sensing technique include good accuracy (better than one centimeter), high reliability, insensitivity to weather conditions, and support for binary coding. The requirement of modifying the infrastructure (installing magnets) and the inherent “look-down” nature (the sensor measures the lateral displacement at locations within the vehicle physical boundaries, versus look-ahead ability) of the sensing system are two known limitations of this technology. The principle idea for this sensing system is straightforward. Magnetic markers are installed under the roadway delineating the center of each lane or any other appropriate lines for the specific applications. Magnetometers mounted under the vehicle sense the strength of the magnetic field as the vehicle passes over each magnet. Onboard signal processing software calculates the relative displacement from the vehicle to the magnet based on the magnetic strength and the knowledge of the magnetic characteristics of the marker. This computation is designed to be insensitive to the vehicle bouncing (e.g., heave and pitch) and the ever-present natural and man-made magnetic noises. Furthermore, the road geometric information can be encoded as a sequence of bits, with each bit corresponding to a magnet. The polarity of each magnet represents either 1 (one) or 0 (zero) in the code. In addition to the lateral displacement measurement and road geometry preview information, other vehicle measurements such as yaw rate, lateral acceleration, and steering wheel angle may also be used to improve the performance of such a lateral guidance system.

### **2.3.2 Magnetic Noise Effects**

Four major noise sources are usually present in the magnetic signal measurements in a typical vehicle operational environment: earth field, local magnetic field distortion, vehicle internal electromagnetic field, and electrical noise.

The most frequent external disturbance is the ever-present earth’s permanent magnetic field, which is usually on the order of 0.5 Gauss. The value of the earth field measured by the magnetometers on the vehicle depends on the location of the vehicle on earth as well as the altitude and orientation of the vehicle. Although the earth magnetic field usually changes slowly, sharp turns and severe braking can quickly change the field measurements along the vehicle axes.

The most serious noise problems are caused by local anomalies due to the presence of roadway structural supports, reinforcing rebar, and the ferrous components in the vehicle or under the roadway. Underground power lines are another source of such local field distortion. Rebar or structural support usually creates a sharp change in the background

magnetic field and sometimes is difficult to identify. Most signal processing algorithms will have some difficulty recovering from such sharp distortions. The ferrous components in the vehicle, on the other hand, can be isolated as long as their locations are fixed with respect to the magnetometers, or are located at a significant distance from the sensors.

A third source of noise comes from the alternating electric fields generated by various motors operating in the vehicle. These motors may include alternator, fan, electric pump, compressor and other actuators. However, their effects vary according to the motor rotational speed and distance from the magnetometers. The higher the motor rpm or the farther it is placed away from the magnetometers, the less the resultant noise. Sometimes modest changes in sensor placement can alter the size of such disturbances.

The last common noise source arises from the electronic noise in the measurement signal itself. Such noise can be created by the voltage fluctuations in the electrical grounding or from the power source. It can also be a result of poor wiring insulation against electromagnetic disturbances. Usually, the longer the wire, the higher such noise. Although low-pass filtering can reduce the magnitude of such disturbances, noticeable degradation of the magnetic sensor signal process algorithm occurs when such noise level exceeds 0.04 Gauss. Digital transmission of magnetic field measurements or local embedded processor is two possible approaches that can significantly reduce such noise.

### **2.3.3 Magnetic Sensing Algorithm**

One of the important attributes of the lateral sensing system is its reliability. Currently, there exist several algorithms designed to detect the relative position between the marker and sensor (magnetometer), as well as to read the code embedded within a sequence of these markers. Three magnetic marker detection and mapping algorithms have been experimented with by PATH. The first is called the “peak-mapping” method that utilizes a single magnetometer to estimate the marker’s relative lateral position when the sensor is passing over the magnet. The second algorithm is the “vector ratio” method that requires a pair of magnetometers to sample the field at two locations. It returns a sequence of lateral estimates in a neighborhood surrounding, but not including the peak. The third is the “differential peak-mapping” algorithm that compares the magnetic field measurements at two observation points to eliminate the common-mode contributions and reconstructs a functional relationship between the differential sensor readings and the lateral position using the knowledge of the sensor geometry. The “peak-mapping” algorithm was selected for the precision docking project because it has been proven effective over a wide range of speeds and has been widely applied in many experimental applications conducted by PATH.

In the Bus operational environment, the magnetic field maps can deviate quite significantly from the theoretical dipole equation prediction because of the massive amount of ferrous material from the bus body structure located just above the magnetometers. Numerical mapping created by empirical data gathering (calibration) is used to create the associated inverse maps. Figures 2.3.1 and 2.3.2 show the front and rear magnetic tables for the 40” bus, respectively. The figures consist of tables of the

seven magnetometers starting from the right side of the bus to the left, designated as follows: right-right, right, center-right, center, center-left, left and left-left. Each table is obtained with two sets of calibration data, one at a lower sensor height (at around 7 inches from the magnetometer to the magnet) and the other at a higher sensor height (at 11 inches from the magnetometer to the magnet). Each half-circle in the table consists of vertical and horizontal fields of the marker that are collected at 2-cm interval of lateral displacement. The magnetic tables clearly depict the nonsymmetrical natural for the magnetic field due the adjacent ferrous material.

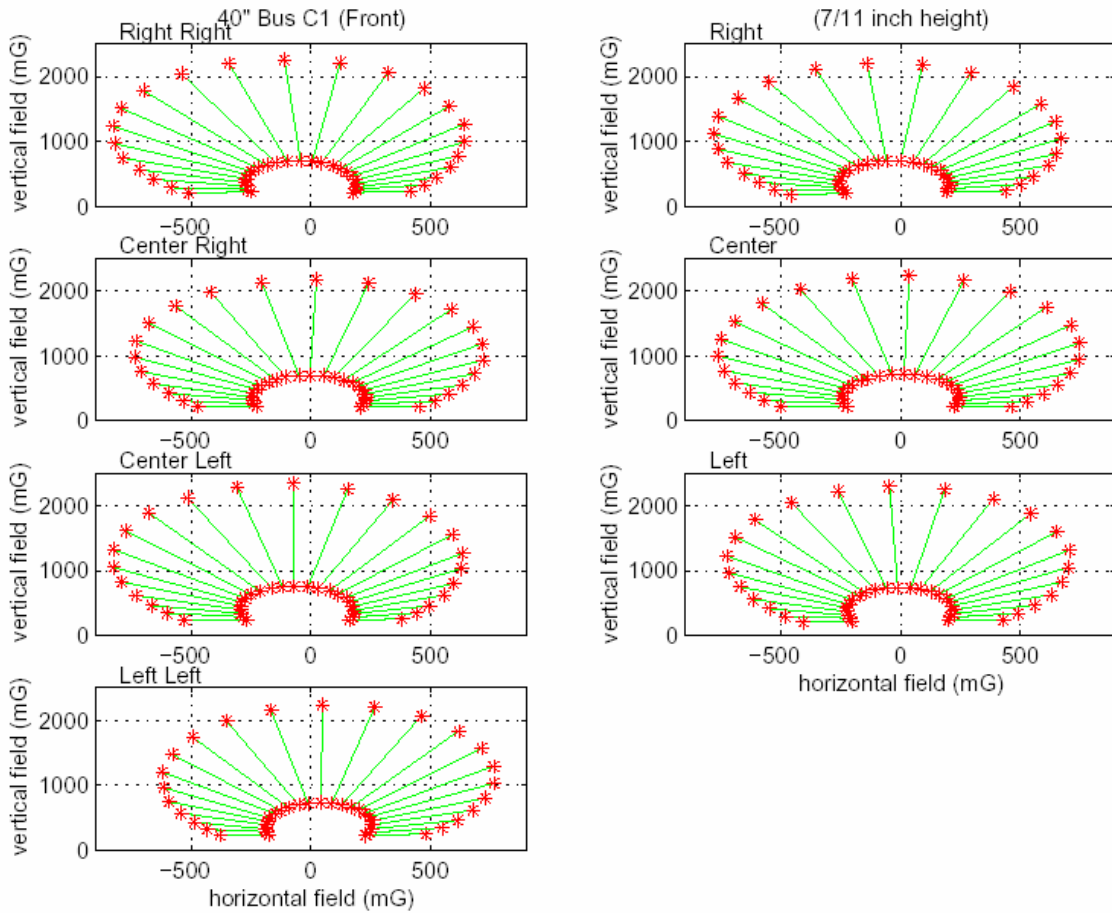


Figure 2.3.1 40" Bus Front Magnetometer Calibration Tables

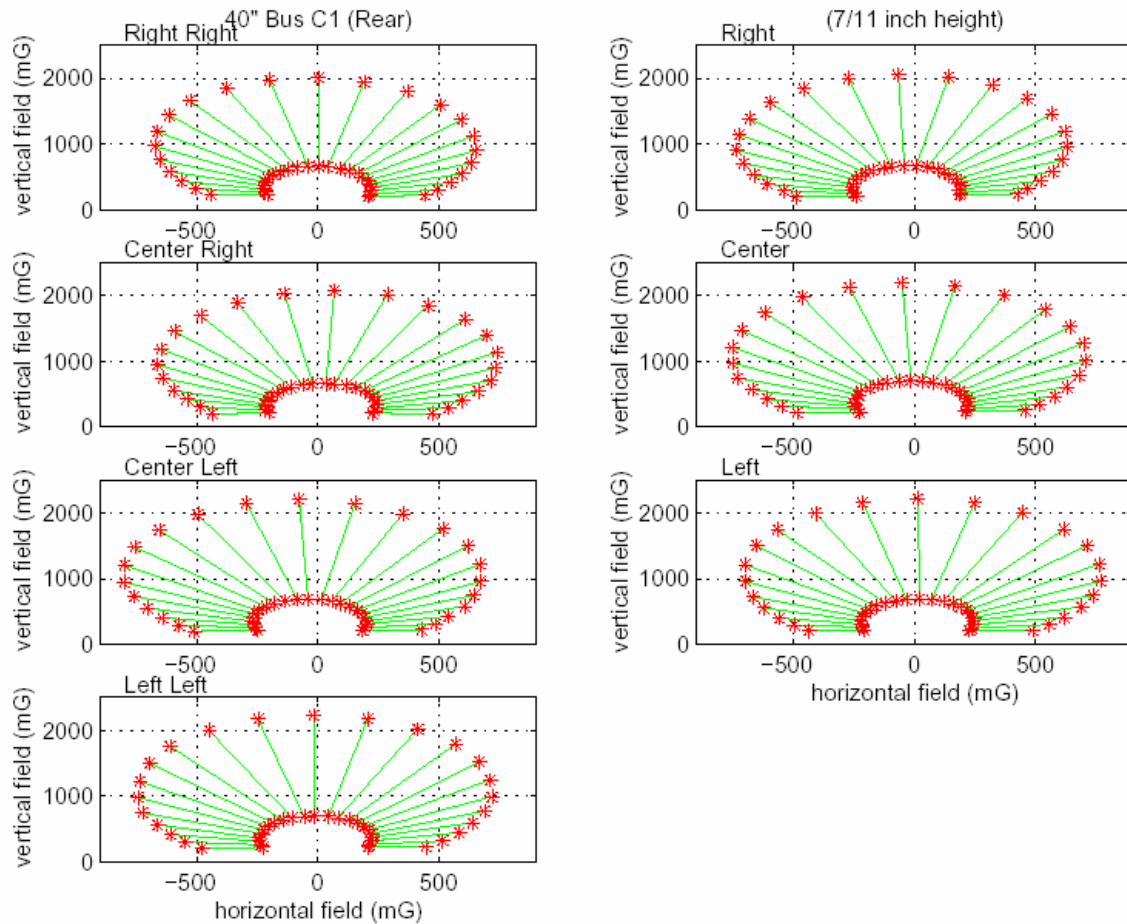


Figure 2.3.2 40" Bus Rear Magnetometer Calibration Table

### 2.3.4 Signal Processing

The magnetometers signal processing for the “peak-mapping” method involves three procedures: peak detection, earth field removal and lateral displacement table look-up (see Figure 2.3.3 for block diagram of signal processing algorithm). Although it is straightforward in principle, it becomes complicated when the reliability of the process is the major concern. Many parameters in the lateral sensing signal processing software need to be tuned in order to provide consistent lateral displacement information regardless of vehicle speeds, orientations, operating lateral offsets and vehicle body motions. Debugging can become very time consuming when failure conditions cannot be recreated. To improve the reliability of the lateral sensing system with the magnetic road markers, PATH has developed a “reconstructive” software system for the lateral sensing signal processing. When specified as a “reconstructive run”, the real-time software in the vehicle, besides processing data as usual, stores all sensor data in memory and later dumps the data into a file. Signal processing software identical to the one run in the real-time environment can later on be generated in a desktop computer using the data stored during vehicle testing as inputs with the same QNX operating system. In such a setup, any erroneous situation can be recreated in a lab environment and debugged with ease.

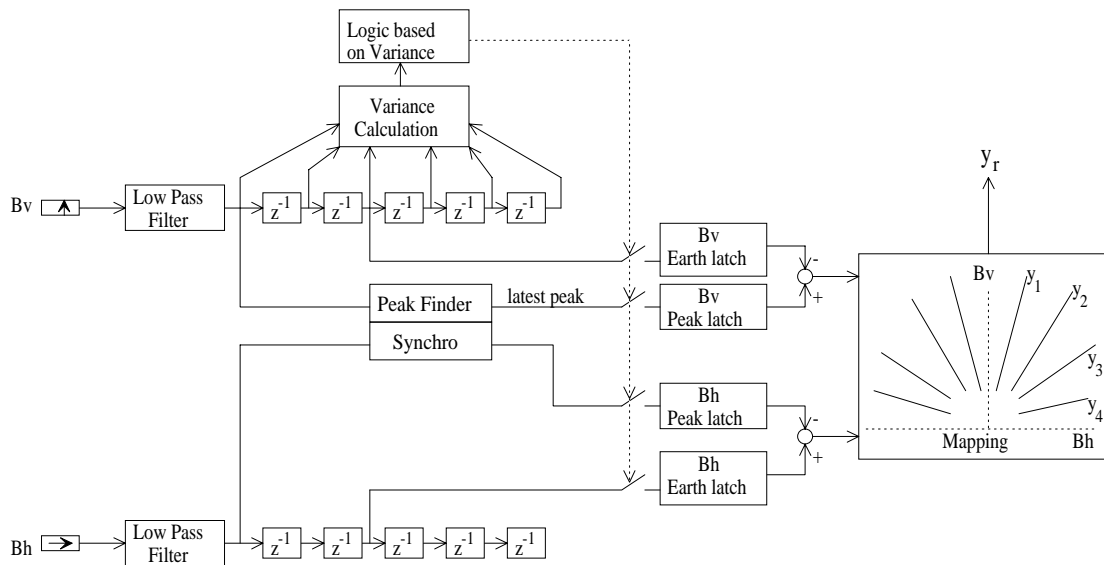


Figure 2.3.3 “Peak-Mapping” Magnetometer Signal Processing Block Diagram

## 2.4 Steering Actuator Design

### 2.4.1 Bus Steering Actuator Requirements

The Top level (closed-loop) steering actuator system requirements are listed as follows:

- **Functionality:**
  - Turn on/off by software
  - Variable driver resistance capability
  - High performance steer position servo
  - Emergency shut-off
  - Ability to impose small force oscillation on hand wheel
- **Performance:**
  - Closed loop servo bandwidth: at least 4 Hz for small amplitude
  - Maximum slew rate: at least 30 degree/sec at the tire (500-600 degree/sec at hand wheel)
  - No oscillation/vibration on hand wheel
  - Position servo accuracy: better than 1 degree at hand wheel
  - Zero position accuracy: better than 1 degree at hand wheel
  - Control Resolution: better than 0.2 degree at hand wheel
- **Safety**
  - Fail to no torque
  - Self diagnosis ability
  - Max torque/rate/power protection

Kill switch

- Installation  
Column installation above assist components  
Low noise level
- Input/output  
Input: steering commands (position or torque), on/off command  
Outputs: steering position(s), actuator status and/or fault flags

The Component level steering actuator (open loop) specifications derived from the top-level requirements are listed as follows:

- Maximum torque: 8-10 N-m
- Maximum slew rate: faster than 25-30 degree/sec at tire (500-600 degree/sec at hand wheel)
- Range: full range of the steering angle
- Position sensor resolution: better than 0.1 degree at hand wheel
- Zero position accuracy: better than 1-2 degree at hand wheel
- Command rate: faster than 100 Hz (if digital), or analog connection between motor circuit and Host computer.
- Time constant for the current/torque command response: faster than 5 ms.
- Fault flag for the open-loop system.
- The motor should be able to be “Back driven” by the driver.

## 2.4.2 Steering Actuator System Configuration

Figure 2.4.1 shows the block diagram of PATH steering actuator. The motor assembly is manufactured by NSK. As shown in Figure 2.4.2 and Figure 2.4.3, steering actuator motor assembly consists of a steering column, DC motor actuating steering column, an electromagnetic clutch and angle sensors measuring steering wheel position. The DC motor connects to the steering column through clutch and reduction gear. An incremental encoder is mounted on the motor shaft to measure the relative position of steering wheel. A multi-turn potentiometer is connected with column shaft via pulley gear and belt to measure the absolute position of steering wheel. Motor current and clutch ON/OFF is controlled by ECU. Upper level computer can also control the clutch by issuing clutch command to ECU. A current loop control is built in ECU as shown in Figure 2.4.4. ECU receives torque command from upper level computer and issues corresponding current command so that DC motor will generate required torque. Strict start and shut down sequences are defined to prevent erroneous operation. ECU has some built-in self-diagnostic features. Failure will be declared when torque command is over allowed limit, power supply to the motor is out of range and motor is overheated. The health condition of motor is feedback to upper level computer through motor condition signal.



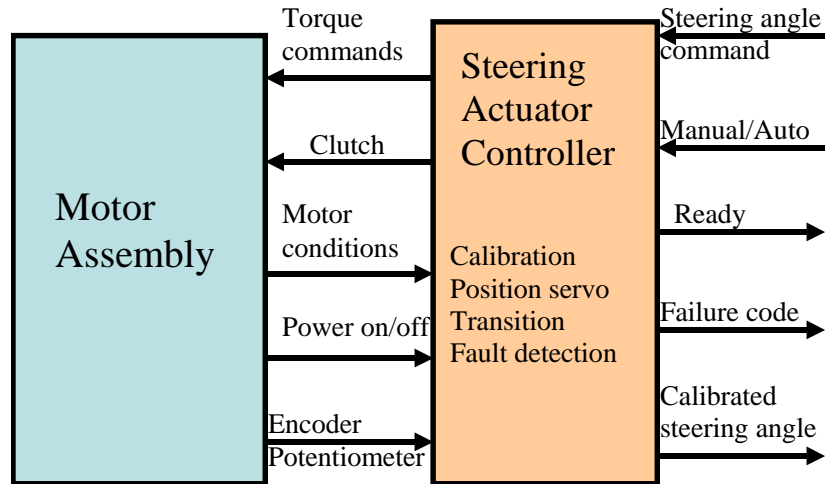


Figure 2.4.1 Block diagram of steering actuator

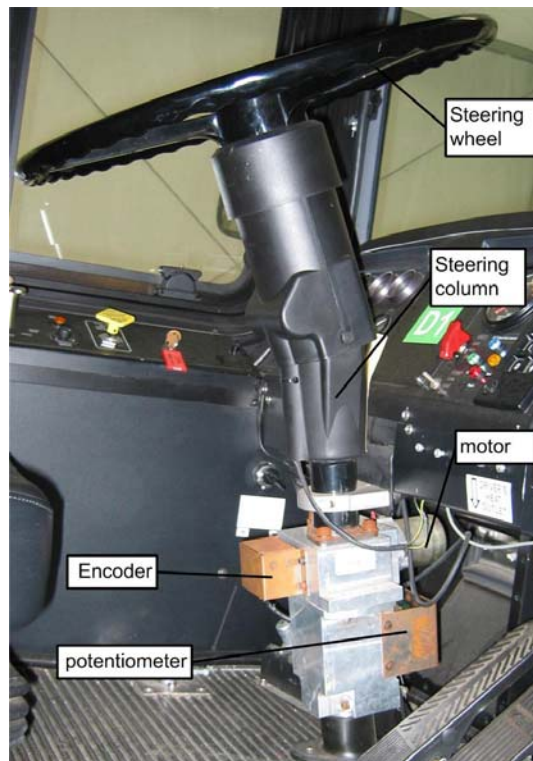


Figure 2.4.2 Steering actuator installation

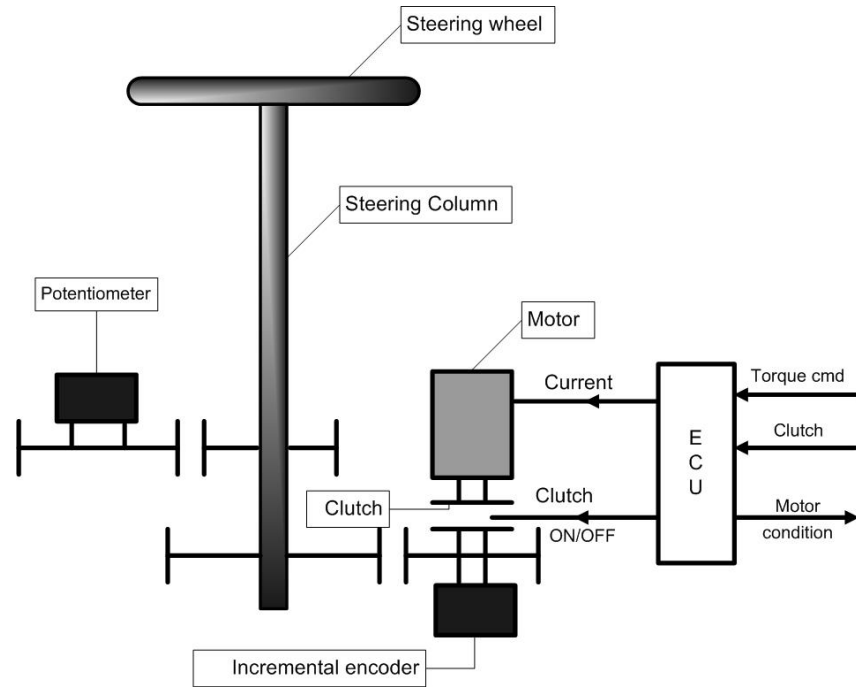


Figure 2.4.3 Schematic of steering actuator motor assembly

Steering actuator controller is a software package designed by PATH researcher which has following functions:

1. Calibration. The function of calibration is to find zero steering angle of the bus.
2. Position servo. Position servo is a closed loop control. It receives steering angle command and issues torque command to steering actuator hardware so that the steering wheel will turn to the desired steering wheel angle position.
3. Smooth transition between manual and automatic control.
4. Fault detection for sensors and motor.

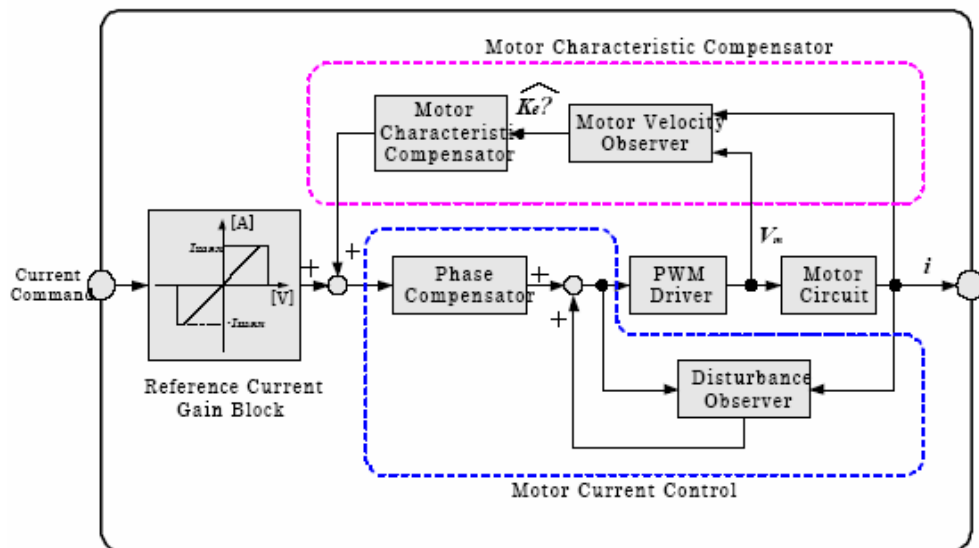


Figure 2.4.4 Current drive loop in ECU

### 2.4.3 Position Servo Design

Position servo is the key function of steering actuator. Successful lateral controller design requires at least 4-5 Hz closed servo loop bandwidth with 1-degree accuracy on steering wheel. Before the servo design can be carried out, extensive experiments are conducted to study open loop characteristics of steering actuator. The experimental results reveal a quite challenging servo design problem. Design of a 40-footer bus steering actuator will be used as an example for illustration purpose.

#### A. Open loop model identification

First, sweep sine technique is used to identify open loop frequency response from torque command (V) to steering wheel angle (degree) with different input amplitudes. As shown in Figure 2.4.5, the open loop bandwidth of 40 footer bus steering actuator is less than 1 Hz. Second, a slow ramp input is sent to study the effect of friction on the road. As shown in Figure 2.4.6, the friction effect is so dominant that the steering wheel starts moving only when torque command almost reaches its half of full capacity (2V). This means the actuating motor is “under powered”. Although this may facilitate driver taking over under emergency situation, the “under powered” motor will pose significant difficulty for servo loop design. This is especially true for low speed application such as precision docking. Third, the steering mechanism of original bus has about 20 degree (steering wheel) of backlash. Such hard nonlinearity, if not properly treated, may lower tracking accuracy, introduce limit cycle or even destabilize whole loop.

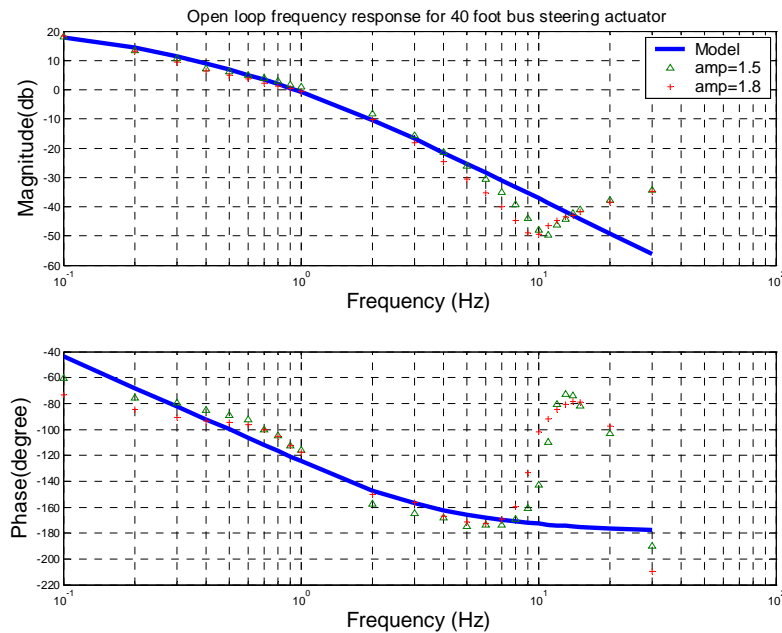


Figure 2.4.5 40 footer bus steering actuator open loop frequency response

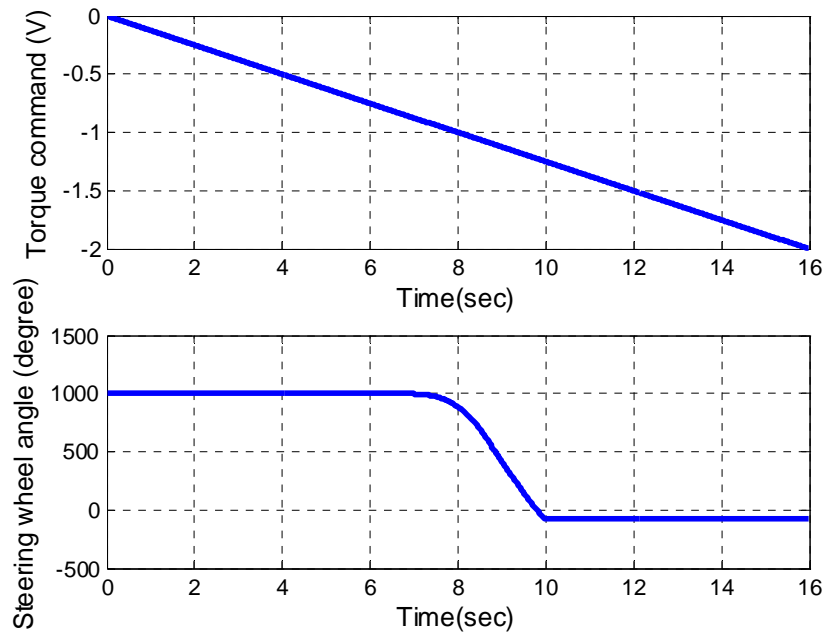


Figure 2.4.6 Friction effect

### B. Closed loop servo design

Figure 2.4.7 shows the closed loop diagram of steering actuator position servo. To address design difficulties mentioned above, different strategies are adopted. First, loop shaping is used to increase closed loop bandwidth as much as possible. In order to overcome friction effect and achieve about 1 degree tracking accuracy up to 4 or 5 Hz, the gain of servo controller has to be sufficient high. However, high gain across all frequency may excite high frequency uncertain dynamics. As shown in Figure 2.4.8, a PD controller is tested first. Although the gain is not high enough to meet 1 degree accuracy requirement, the response already shows a high frequency chattering. Therefore, the frequency response of servo controller needs to be carefully shaped to meet stringent performance requirement and avoid exciting high frequency uncertain dynamics simultaneously.

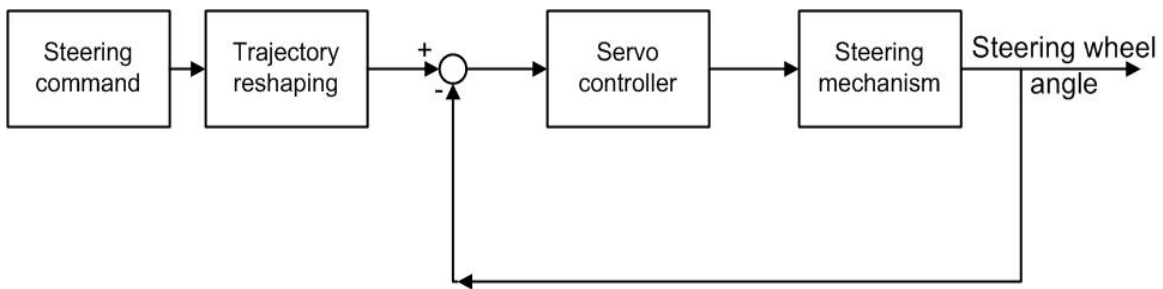


Figure 2.4.7 Closed loop diagram of steering actuator position servo

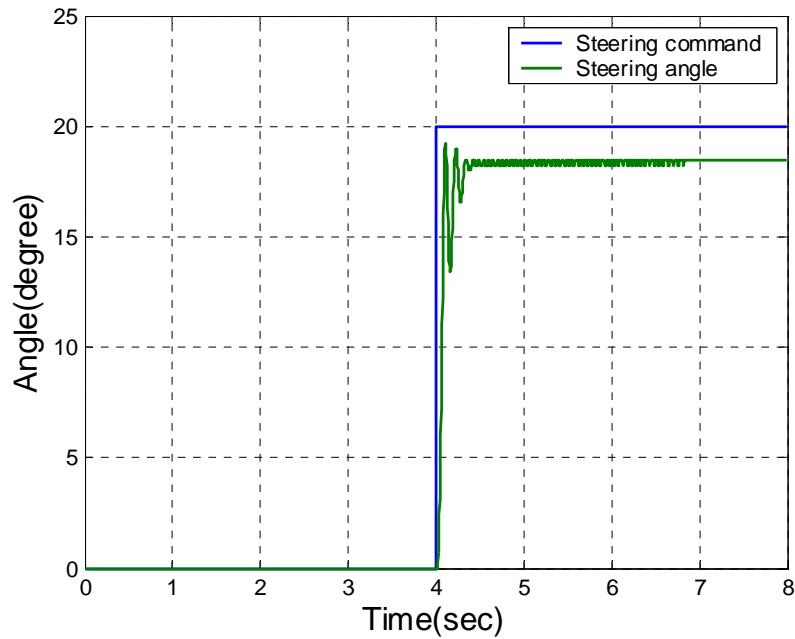


Figure 2.4.8 Step input of a PD controller

After loop shaping design, a baseline high gain linear servo controller that satisfies different performance requirement under most scenarios is obtained. The next step is to take care of different nonlinear phenomena which may have some impacts on system performance under certain conditions. The friction effect will be studied first. Although the gain is high enough to overcome friction and bring tracking error within required 1 degree range as shown in Figure 2.4.9, the friction can still slow system response when command input amplitude is small. Friction compensation is added to speed response as shown in Figure 2.4.10. An adaptive feature is also used to accommodate friction changes due to different road conditions.

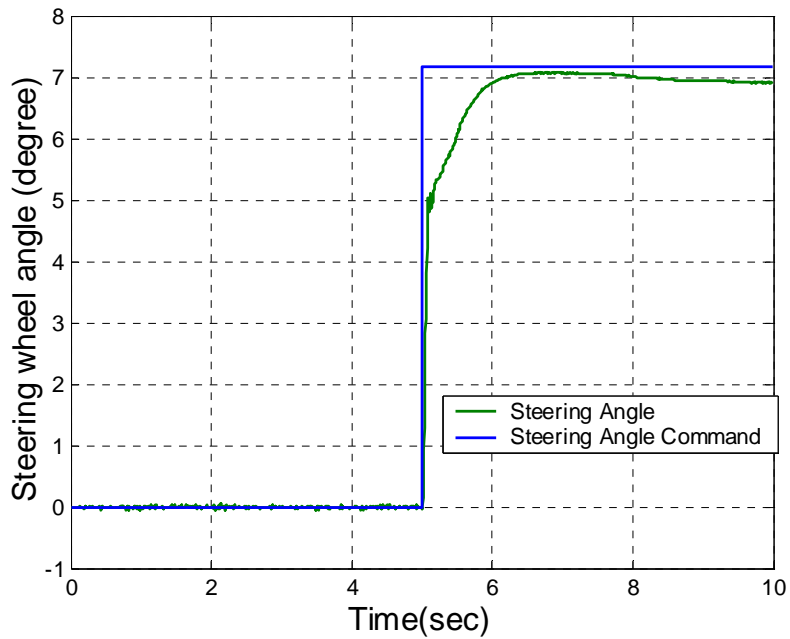


Figure 2.4.9 Friction effect for small amplitude command

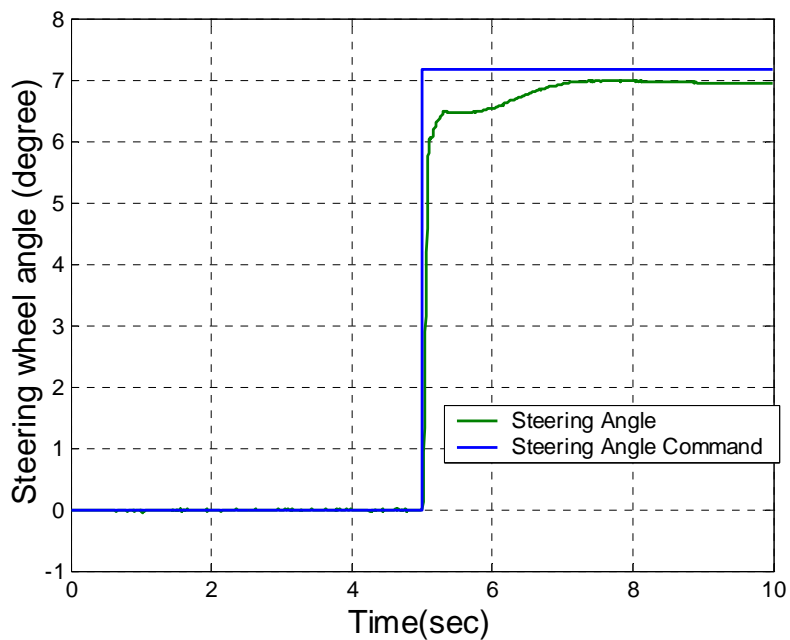


Figure 2.4.10 Step input with friction compensation

In our actuator design, the motor torque command is always saturated due to its “under powered” nature. Such saturation may cause large overshoot as shown in Figure 2.4.11 when command is large. A trajectory reshaping technique and low-and-high gain design are used to address such windup problem. Figure 2.4.12 shows the step input result with anti-windup design. Under this design, the overshoot disappears.

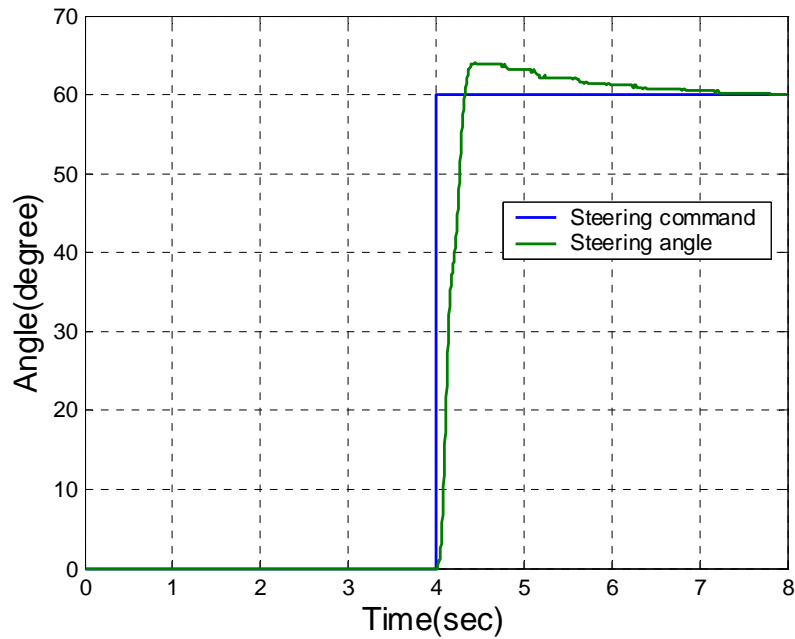


Figure 2.4.11 Overshoot when command input is large

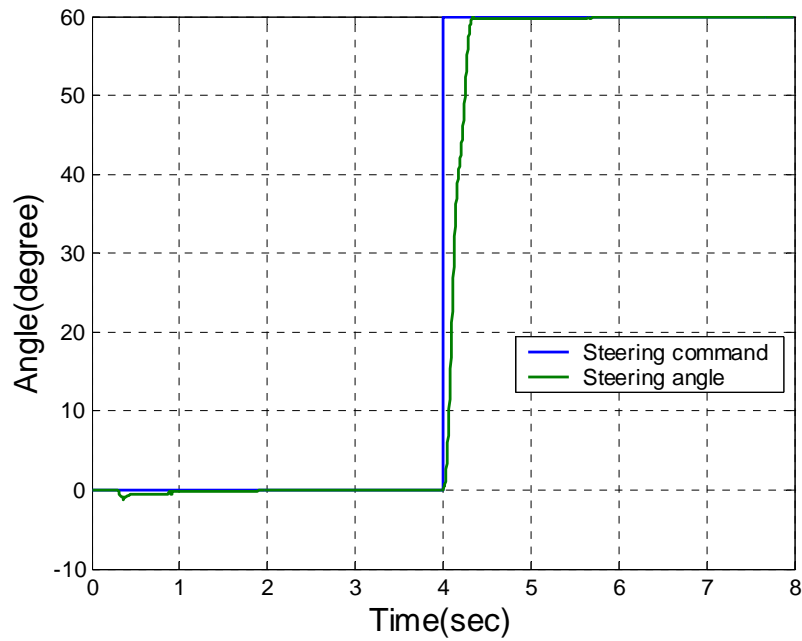


Figure 2.4.12 Step input with anti-windup

As we mentioned before, 20-degree backlash exists in the bus steering mechanism. Limit cycle in form of small oscillations around equilibrium point is generated due to the backlash (Figure 2.4.13). Such oscillation generates high frequency sound and may shorten the life of steering actuator. A nonlinear compensation is used to eliminate such limit cycle and result is shown in Figure 2.4.14.

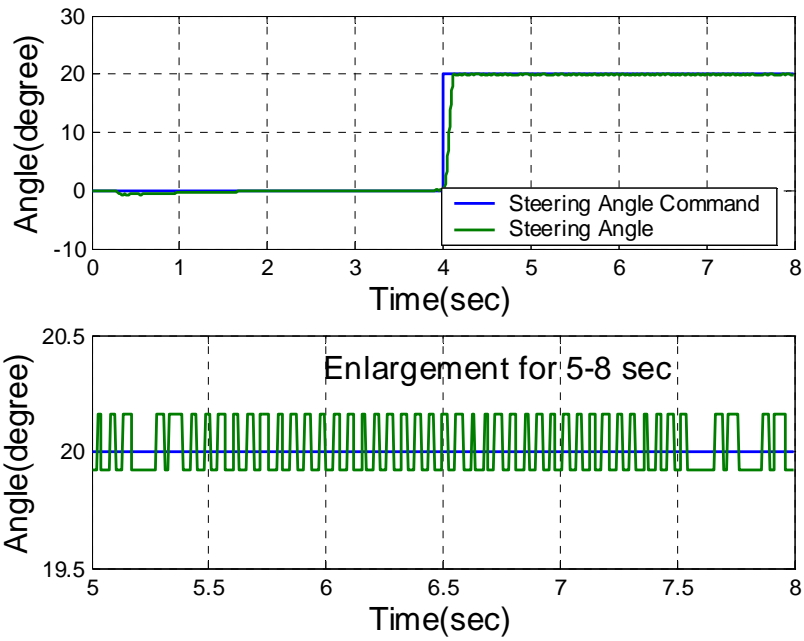


Figure 2.4.13 Limit cycle due to backlash in the steering mechanism

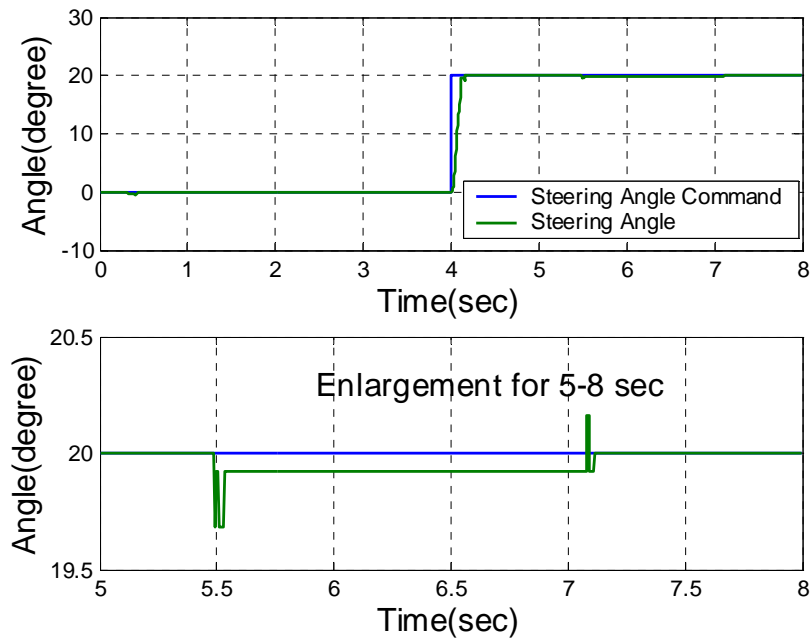


Figure 2.4.14 Limit cycle eliminated

The final closed loop frequency response is shown in Figure 2.4.15 with 6-7 Hz bandwidth.



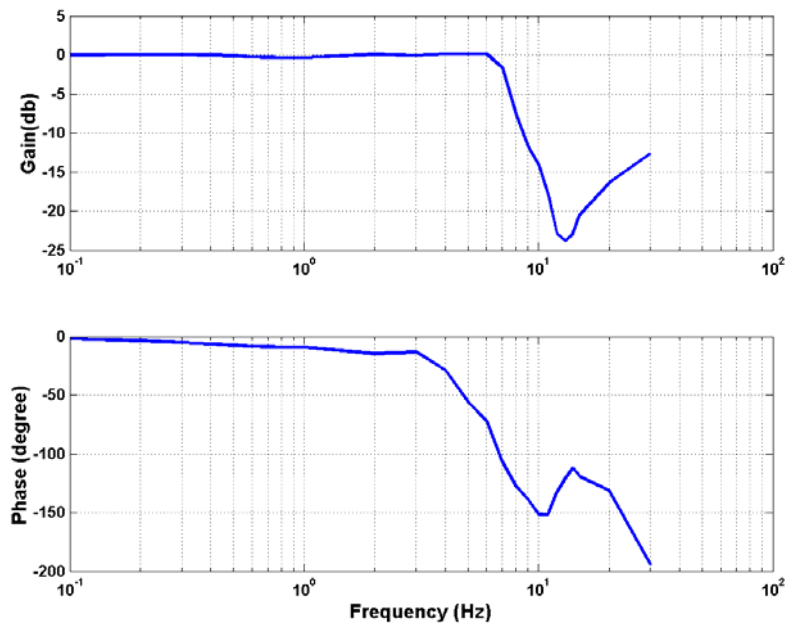


Figure 2.4.15 Closed loop response

## 2.5 Precision Docking Lateral Controller Design

### 2.5.1 Practical Issues In Designing Steering Control

Safety is the first consideration of any transportation system design. Extreme reliability and robustness is the fundamental requirement for any automatic vehicle control system. In general, an ideal automatic vehicle control system should be extremely reliable, with good ride quality, long life cycle, and relatively low cost. In addition, the fact that almost everyone has either ridden in or driven a car creates an unusual obstacle in designing an automated vehicle. Since most people can differentiate between good drivers from bad ones, they will naturally demand a good ride quality for any automatic vehicle. By human nature, for example, bad performance, even during a 2-second duration, can create a stronger impression than a 1-hour good ride could. In that sense, the automatic vehicle controller has to perform under all the “uncommon” scenarios, and improve any “worst” performance as much as possible.

To design any optimal system, the development procedure is often adopted to the specific problem. Control synthesis is selected according to its appropriateness to the sensing system, the plant dynamics and the performance requirements. In the design of the current PATH docking control algorithm, a lateral referencing system based on roadway magnet markers is chosen as the default sensing system. Such sensing systems are generally of simpler nature and are more reliable because of the short distance between the sensors and the markers. However, it does impose stringent design requirement for the controller since “look-down” systems typically do not provide enough “phase lead” for adequate high-speed steering control. Discrete markers may also adversely affect low-

speed's accuracy and smoothness. Furthermore, vehicle dynamics vary greatly across different operational velocities, and this issue must be addressed by any controller design.

This Section focuses on the design of a robust steering controller based on roadway markers. In particular, it shows that a single controller is adequately to the general steering control problem under various operating conditions without switching between different controllers. Such switching in practice can be very problematic. And such controller, if achievable, would be a better system choice because it's simultaneous suitability with multiple steering control scenarios.

## **2.5.2 Control Problem Formulation**

### **A. Performance Requirements**

A bus precision docking control system is a subset of an automated steering control system for a Bus Rapid Transit application. An automated steering control system targeted toward a Bus Rapid Transit application is required to perform all normal steering functions from leaving a bus station to arriving at a bus station with extremely high reliability. It should be robust against different roadway geometries, unknown vehicle loading, various speeds, and changing roadway surface conditions. An ideal element of such automated steering control system is a high-gain robust "vehicle lateral servo" that "steers" the vehicle to follow any desired trajectory as long as such trajectory is defined within the limitations of the vehicle capabilities. The closed-loop performance requirements for a general Bus automated steering control algorithm are defined as follows:

1. 0.2 meter maximum tracking error for highway driving without any prior knowledge of the roadway
2. 0.5 meter maximum tracking error for 0.3-g automated steering maneuver without any prior knowledge of the roadway
3. 0.02 meter maximum tracking error for vehicle speed less than 5 m/s on straight sections of the roadway for docking accuracy
4. No noticeable oscillations at frequencies above 0.3 Hz for passenger comfort, and 0.4 minimum damping coefficient for any mode at lower frequencies
5.  $1 \text{ m/s}^2$  maximum lateral acceleration deviation between the lateral acceleration created by the vehicle and that from the road
6. Consistent performance under various vehicle-operating conditions

Requirements 1, 2 and 6 address scenarios other than precision docking. They are included simply because that a "precision docking ready" controller should also be "Bus Rapid Transit ready." They use virtually the same vehicle and infrastructure components.

In addition to the above performance requirements, a design preference was imposed for the controller structure: a uniform control structure is preferable since it will not require transition between different controllers. The transitions between different controllers usually increase the complexity of the controller design, and often reduce the robustness of the overall system. This design preference pushes for a single controller that works for all normal bus operating scenarios without any transitioning between different control configurations.

## B. Vehicle Mode

Many researchers use bicycle model for vehicle steering control. However, most buses have a relatively soft suspension. The soft suspension significantly alters the frequency characteristics of the lateral vehicle dynamics from that predicted by the bicycle model. In order to study the influence of the suspension roll dynamics on the steering control design, a 3 DOF vehicle model that includes lateral, yaw and roll dynamics is used for the controller design. The schematic diagram of the 3 DOF vehicle model is shown in Figure 2.5.1. The sprung mass ( $m_s$ ) interacts with the front and rear unsprung masses via the front and the rear suspensions, where  $K_f, D_f$  and  $K_r, D_r$  are the rotational spring and damper coefficients for front and rear suspension, respectively. The roll axis is defined as the line connecting the roll centers of the front and rear suspension as shown in Figure 2.5.1. It can be found that the vehicle geometric parameter that affects the coupling between lateral and roll dynamics the most is  $h_{m_s}$ , the distance between the sprung mass CG and the roll axis. Additional vehicle parameters are defined as follows:  $\beta$  is the side slip angle between vehicle longitudinal axis, velocity vector  $v$  at CG, and  $\dot{\psi}$  the vehicle yaw rate. Other parameters:  $\delta_f$  the front steering angle,  $I_\psi$  the yaw moment of inertia,  $M$  the mass of the vehicle,  $l=l_f+l_r$  the wheel base,  $c_f$  and  $c_r$  the linear cornering stiffness of the front and rear tires, respectively.

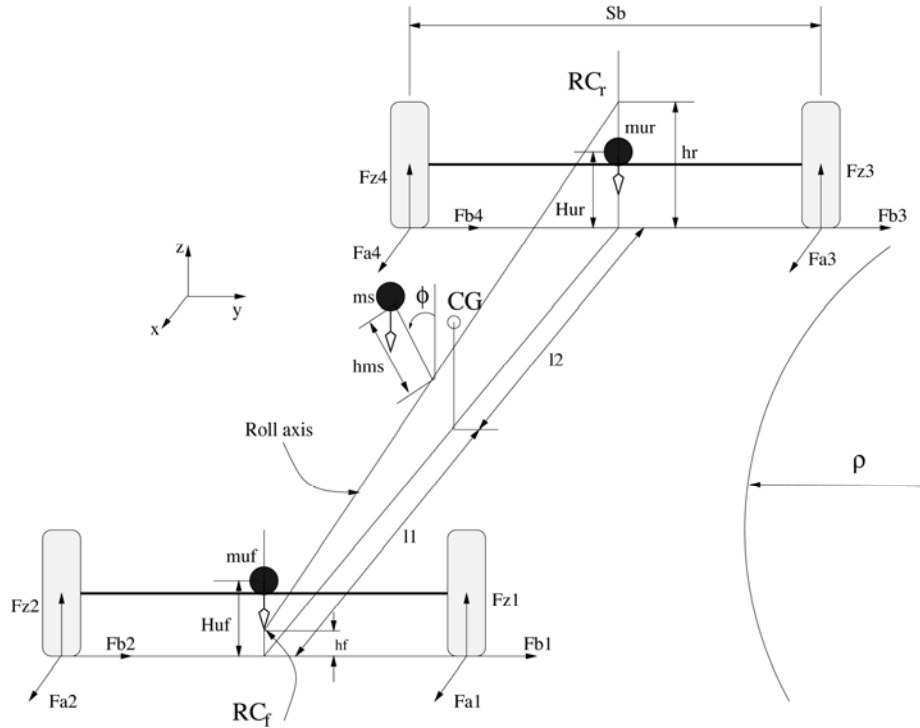


Figure 2.5.1 Schematic diagram of 3 DOF vehicle model

Under constant speed condition, the dynamic equations of motion are derived using the Newtonian method. Assuming small angles and using the linear tire model, the linear dynamics equations of the vehicle model with respect to the road reference frame are derived and shown in Eq. (2.1). The state-space representation takes the form of  $\dot{\bar{x}} = A\bar{x} + B\delta + \bar{d}$ . The state variables are:  $y_r, \dot{y}_r$ , the lateral displacement at CG w.r.t. road reference frame and its derivative;  $\psi_r, \dot{\psi}_r$ , the yaw angle w.r.t. the road reference frame and its derivative; as well as  $\phi_r, \dot{\phi}_r$ , the roll angle and its derivative. The road reference frame is attached to the road center at a point adjacent to the vehicle CG with X axis tangent to the road trajectory and moves along the road with the same speed as the vehicle. The input is the front steering angle ( $\delta$ ). The disturbances are:  $\rho$ , the road curvature;  $\dot{\psi}_d$ , the desired yaw rate from the road;  $F_{wy}$ , the disturbance force at CG along the y direction; and  $F_x$ , the front tire force along the tire orientation. Since no bus parameters were not available during the design process, parameters gathered from various sources were used for the control design purposes. It turned out that the final controller parameters were close enough to those resulted from the “general vehicle parameters” due to the robust design method. Only a couple “tuning” steps within two days came the final design parameters.

$$\frac{d}{dt} \begin{bmatrix} y_r \\ \& \\ \psi_r \\ \& \\ \phi_r \\ \& \end{bmatrix} = \begin{bmatrix} 0 & 1 & 0 & 0 & 0 & 0 \\ 0 & \frac{A_1\Lambda_1}{v} & -A_1\Lambda_1 & \frac{A_2\Lambda_1}{v} & R_1 & R_2 \\ 0 & 0 & 0 & 1 & 0 & 0 \\ 0 & \frac{A_3}{v} & -A_3 & \frac{A_4}{v} & R_3 & 0 \\ 0 & 0 & 0 & 0 & 0 & 1 \\ 0 & \frac{A_1\Lambda_2}{v} & -A_1\Lambda_2 & \frac{A_2\Lambda_2}{v} & R_4 & R_5 \end{bmatrix} \begin{bmatrix} y_r \\ \& \\ \psi_r \\ \& \\ \phi_r \\ \& \end{bmatrix} + \begin{bmatrix} 0 \\ B_1\Lambda_1 \\ 0 \\ B_2 \\ 0 \\ B_1\Lambda_2 \end{bmatrix} \delta + \begin{bmatrix} 0 \\ d_1 \\ 0 \\ d_2 \\ 0 \\ d_3 \end{bmatrix} \quad (2.1)$$

where the coefficients are defined as follows:

$$\begin{aligned} A_1 &= -\frac{2(c_f + c_r)}{M}, \quad A_2 = \frac{2(-l_f c_f + l_r c_r)}{M}, \quad A_3 = \frac{2(-l_f c_f + l_r c_r)}{I_\psi}, \\ A_4 &= \frac{-2(l_f^2 c_f + l_r^2 c_r)}{I_\psi}, \quad \Lambda_1 = \frac{MI_{x_s}}{MI_{x_s} - m_s^2 h_{m_s}^2}, \quad \Lambda_2 = \frac{Mm_s h_{m_s}}{MI_{x_s} - m_s^2 h_{m_s}^2}, \\ R_1 &= \frac{2(\gamma_f + \gamma_r)I_{x_s} + m_s h_{m_s} (m_s g h_{m_s} - K_f - K_r)}{MI_{x_s} - m_s^2 h_{m_s}^2}, \quad R_2 = \frac{-m_s h_{m_s} (D_f + D_r)}{MI_{x_s} - m_s^2 h_{m_s}^2}, \\ R_3 &= \frac{2(\gamma_f l_f - \gamma_r l_r)}{I_\psi}, \quad R_4 = \frac{2m_s h_{m_s} (\gamma_f + \gamma_r) + M(m_s g h_{m_s} - K_f - K_r)}{MI_{x_s} - m_s^2 h_{m_s}^2}, \\ R_5 &= \frac{-M(D_f + D_r)}{MI_{x_s} - m_s^2 h_{m_s}^2}, \quad B_1 = \frac{2(c_f + F_x)}{M}, \quad B_2 = \frac{2l_f (c_f + F_x)}{I_\psi}, \\ d_1 &= \frac{\Lambda_1}{M} F_{wy} + \frac{A_2 \Lambda_1}{v} \& - v^2 \rho, \quad d_2 = -\frac{2(-l_f^2 c_f + l_r^2 c_r)}{I_\psi v} \&, \\ d_3 &= \frac{\Lambda_2}{M} F_{wy} + \frac{A_2 \Lambda_2}{v} \& - 2\Lambda_2 v^2 \rho \end{aligned} \quad (2.2)$$

### C. Control Problem Formulation

Since most vehicle lateral sensing systems provide lateral measurement at a certain sensor location, the control formulation starts with using a typical such lateral measurements for steering control. Assuming this measurement is taken at a location  $d_s$  meters in front of CG, the lateral displacement at the sensor location can be written as

$$y_s = y_r + d_s \psi + h_s \phi, \quad (2.3)$$

where  $h_s$  is the distance from the sensor to the roll axis. Differentiating Eq. (2.3) twice and assuming  $v$  is constant, the vehicle lateral acceleration transfer function at the sensor location S,  $V_s(s)$ , is derived by using Eq. (2.1) as

$$y_s(s) = \frac{V_s(s)}{s^2} \delta_f(s) = \frac{1}{s^2} \left( s \begin{bmatrix} 0 & 1 & 0 & d_s & 0 & h_s \end{bmatrix} (sI - A)^{-1} B \right) \delta_f(s). \quad (2.4)$$

Alternatively,  $V_s(s)$  can be defined as

$$V_s(s) = sG_{\&,\delta}(s) + d_s sG_{\psi,\delta}(s) + h_s sG_{\phi,\delta}(s) \quad (2.5)$$

where  $G_{\delta}(s)$ ,  $G_{\psi\delta}(s)$  and  $G_{\phi\delta}(s)$  are transfer functions from steering angle to  $\delta$ ,  $\psi$  and  $\phi$ , respectively.

Figure 2.5.2 depicts a generic block diagram of a steering feedback system based on lateral displacement measurement. The vehicle lateral model consists of five subsystems: actuator dynamics ( $A(s)$ ), road reference (desired lateral acceleration at the sensor location:  $\delta_{ref} = v^2 \rho$ ), vehicle dynamics at sensor ( $V_S(s)$ ), vehicle kinematics ( $1/s^2$ ) and control law ( $C(s)$ ). The goal of steering control synthesis is to determine a control law  $C(s)$  that is capable of stabilizing the vehicle lateral dynamics with sufficiently high gains to satisfy the performance requirements. One major challenge in choosing the controller  $C(s)$  is to maintain enough stability margins under the delays and uncertainties from  $V_S(s)$  and  $A(s)$ .

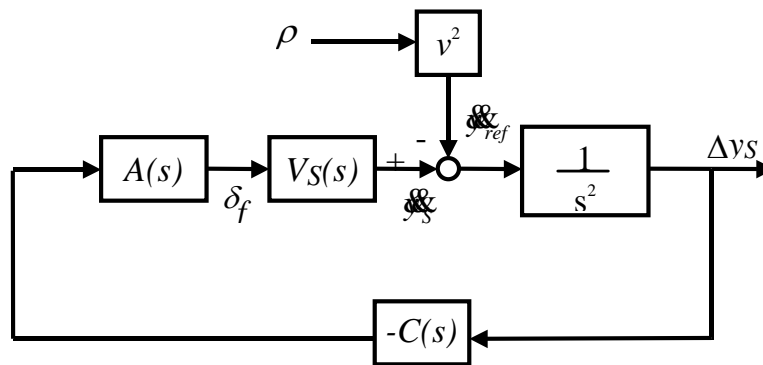


Figure 2.5.2 Vehicle steering control block diagram

### 2.5.3 Basic Steering Controller Design

#### A. Controller Requirements

The stability and performance requirements are examined for the simplified steering closed-loop system described in Figure 2.5.2 as

$$\Delta y_s(s) = \frac{1}{s^2 + A(s)V_S(s)C(s)} v^2 \rho(s). \quad (2.6)$$

In order to prevent excessive steering oscillation, sufficient phase margin ( $pm$ ) and gain margin ( $gm$ ) are required for the above system:

$$\angle \frac{A(j\omega_p)V_S(j\omega_p)C(j\omega_p)}{\omega_p^2} > -(\pi - pm), \quad \text{at} \quad \left| \frac{A(j\omega_p)V_S(j\omega_p)C(j\omega_p)}{\omega_p^2} \right| = 1; \quad (2.7)$$

as well as

$$\left| \frac{A(j\omega_g)V_S(j\omega_g)C(j\omega_g)}{\omega_g^2} \right| < \frac{1}{gm}, \quad \text{at} \quad \angle \frac{A(j\omega_g)V_S(j\omega_g)C(j\omega_g)}{\omega_g^2} = -\pi. \quad (2.8)$$

In order to maintain a tight lane-keeping ability, the following lane-tracking requirement is imposed:

$$|\Delta y_s(t)| \leq K_a \max(v^2 | \rho |). \quad (2.9)$$

The requirement in Eq. (2.9) guarantees that the lateral displacement deviation ( $\Delta y_s$ ) shall not exceed  $K_a$  meters from a  $1 \text{ m/s}^2$  step input of the reference road acceleration ( $v^2 \rho$ ). By using the inequality

$$|\Delta y_s(t)| = L^{-1} \left\{ \frac{1}{s^2 + A(s)V_s(s)C(s)} \frac{v^2 \rho}{s} \right\} \leq \sup_{s=j\omega} \left( \left| \frac{1}{s^2 + A(s)V_s(s)C(s)} \right| \right) \max(v^2 \rho) \quad (2.10)$$

where  $L^{-1}$  denotes the inverse Laplace transform, Eq. (2.10) can be rewritten as

$$\left| \frac{1}{s^2 + A(s)V_s(s)C(s)} \right|_{s=j\omega} \leq K_a. \quad (2.11)$$

Eqs. (2.7), (2.8) and (2.11) are the basic design requirements for the controller  $C(s)$ .  $C(s)$  needs to supply the necessary phase lead (minimum phase margin plus system delays) at gain-crossover frequency based on Eq. (2.7); and Eq. (2.11) indicates that this crossover frequency increases as  $K_a$  decreases. Figure 2.5.3 plots the required phase lead at the gain crossover frequency for  $C(s)$  with respect to different vehicle speeds using a typical 3 DOF vehicle model. According to Figure 2.5.3, as the vehicle speed goes above 30 m/s and  $d_s = 0 \text{ m}$ ,  $C(s)$  is required to deliver at least 100 degrees phase lead when  $\omega_p$  is chosen around 1 Hz, a critical range for high speed operation. This observation suggests that a lateral sensing system that produces only lateral measurement near the vehicle CG creates a stringent design problem for a robust steering controller at high speeds. On the other hand, this constraint is greatly reduced when the lateral deviation is measured at some distance in front of the vehicle. Figure 2.5.3 also shows the corresponding required phase lead for  $C(s)$  when the measurement is taken 5 meters in front of CG. In such case, only 20-degree phase lead at  $\omega_p = 1 \text{ Hz}$  is required. A simple lead-lag compensator for the output  $\Delta y_s$  suffices to stabilize the closed-loop steering control system at high speeds.

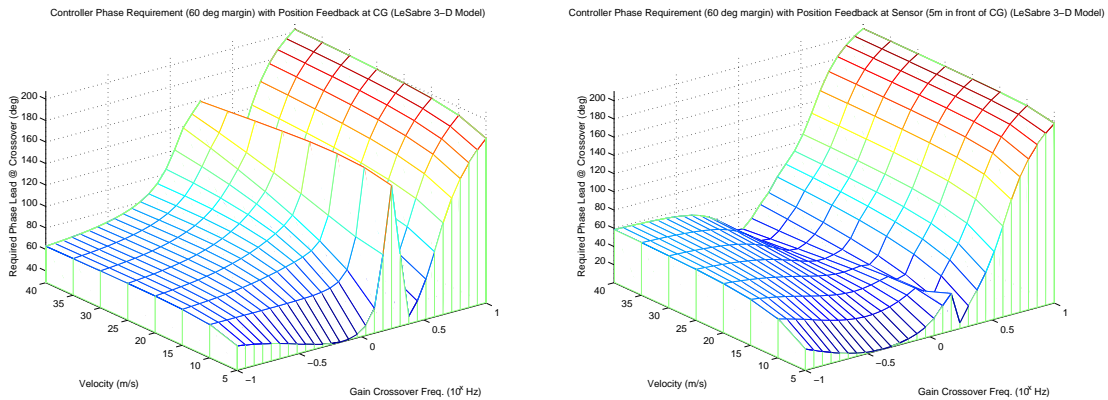


Figure 2.5.3 Controller phase requirement (60 degree phase margin) at gain crossover frequency: (a) Left:  $d_s = 0 \text{ m}$ ; (b) Right:  $d_s = 5 \text{ m}$ .

## B. Look-ahead Steering Controller

The analysis the section above suggests that the generic vehicle steering controller depicted by Figure 2.5.2 is a good candidate for steering controller design. According to Eq. (2.5), the “look-ahead” distance  $d_s$  can be regarded as an additional “control parameter” along with the parameters of  $C(s)$ . To investigate the effects of this extra degree of freedom with respect to the steering controller design, the simple closed-loop structure with two constant control gains ( $d_s$  and  $C(s) = k_c$ ) is chosen at any given vehicle velocity in this section as in Eq. (2.13):

$$\Delta y_s(s) = \frac{1}{s^2 + A(s)V_S(s, d_s)k_c} v^2 \rho(s). \quad (2.13)$$

The following optimization technique is then derived to obtain the optimal control gains that attain the closed loop requirements (2.7), (2.8) and (2.11):

For every vehicle speed  $v$  and for any given  $d_s$ , the maximum attainable phase margin,  $\beta_{\max}(d_s, v)$ , is obtained as

$$\beta_{\max}(d_s, v) = \max_{\omega \in \mathbb{R}} \left( \angle(A(j\omega)V_S(j\omega, d_s, v)) \right), \quad (2.14)$$

$$\left| \frac{A(j\omega_g)V_S(j\omega_g, d_s, v)\omega_p^2}{A(j\omega_p)V_S(j\omega_p, d_s, v)\omega_g^2} \right| \leq \frac{1}{gm}$$

where the frequencies  $\omega_p$  and  $\omega_g$  are determined by

$$\angle(A(j\omega_g)V_S(j\omega_g, d_s, v)) = 0, \quad (2.15)$$

$$\beta_{\max}(d_s, v) = \angle(A(j\omega_p)V_S(j\omega_p, d_s, v)). \quad (16)$$

The local optimal choice of  $k_c$  that results in the maximum attainable phase margin,  $\beta_{\max}(d_s, v)$ , for a given  $d_s$  is defined by

$$k'_c(d_s, v) = \left| \frac{-\omega_p^2}{A(j\omega_p)V_S(j\omega_p, d_s, v)} \right|. \quad (2.17)$$

The optimal choice of the control gain pair  $(\bar{k}_c(v), \bar{d}_s(v))$  that satisfies the stability requirements (2.7) and (2.8) for any given vehicle speed  $v$  is calculated as

$$\bar{k}_c(v) = \max_{d_s \in \mathbb{R}, \beta_{\max}(d_s, v) > pm} (k'_c(d_s, v)) = k'_c(\bar{d}_s(v), v). \quad (2.18)$$

Finally, the lane-tracking performance is examined by using Eqs. (2.11) and (2.18) as

$$\left| \frac{1}{s^2 + A(s)V_S(s, \bar{d}_s(v), v)\bar{k}_c(v)} \right|_{s=j\omega} \leq K_a(v). \quad (2.19)$$

Since Eq. (2.19) usually provides a rather conservative estimate, an alternative method for a more precise error bound is to directly compute the maximum transient error with respect to a  $1 \text{ m/s}^2$  step road acceleration input through inverse Laplace transformation. Figure 2.5.4 shows the maximum attainable phase margin ( $\beta_{\max}$ ) based on Eq. (2.14) and the local optimal control gain ( $k'_c$ ) as in Eq. (2.18) using 2 as the minimum gain margin



(*gm*). The plot of  $\beta_{\max}$  confirms that increasing the look-ahead distance does improve the attainable maximum phase margin to within the requirements; the plot of  $k'_c$  suggests that higher gain is possible at low speeds.

Figure 2.5.5 displays the optimal control gain pair  $(\bar{k}_c(v), \bar{d}_s(v))$  computed by Eq. (2.18), Figure 2.5.6 shows the resultant maximum transient error and error bound ( $K_a$  by Eq. (2.19)). These optimal gain pairs guarantee at least 50-degree phase margin ( $pm$  is set for 50 degrees in the above computations) and gain margin of 6 db for each vehicle speed. Initial observation of Figure 2.5.5 reveals two phenomena that follow engineering intuition: (1) the optimal look-ahead distance increases as the speed increases; (2) the larger the look-ahead distance, the smaller the feedback gain; (3) large feedback gain is required at very low vehicle speeds. It is interesting to notice from Figure 2.5.5 that a look-ahead distance of about 1 to 2 car-length is generally adequate for steering control. It is straightforward to show that the smooth optimal gain curves assure the robustness of the “gain-scheduling” algorithm with respect to speed variations.

Figure 2.5.6 illustrates the lane-tracking ability of the optimal gain pairs. The gain pairs result in 18 cm maximum tracking error (including transient) for every 0.1g lateral road disturbance without any prior knowledge of road curvature. It demonstrates the possibility of using constant feedback gain with constant look-ahead distance to achieve all lane-tracking requirements specified in Section 3.1 at any speed.

Figure 2.5.4 further indicates that the attainable phase margins between 30 and 40 m/s are larger than those between 10 and 20 m/s. This characteristics is somewhat counter intuitive. Under constant look-ahead distance, the coupling among lateral, yaw and roll of the test vehicle requires the controller to provide more phase lead around 1 Hz when the vehicle speed is between 10 and 20 m/s (as seen in figure 2.5.3). The need for larger phase lead results in larger  $\bar{k}_c(v)$  and smaller  $\bar{d}_s(v)$  at vehicle speeds between 10 and 20 m/s, as well as larger transient error around 10 m/s. A frequency shaped look-ahead distance ( $G_{ds}(s)$ ) can relax such limitation and will be discussed in the previous sections.

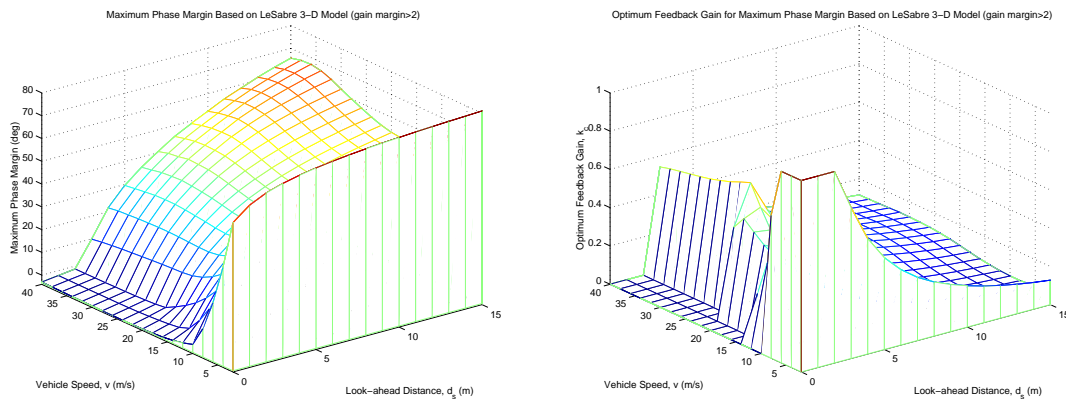


Figure 2.5.4 Maximum attainable phase margin and optimal gain based on 3 DOF model with constant control parameters  $(k_c, d_s)$ , ( $gm=2$ ): (a) Left:  $\beta_{\max}$ ; (b) Right:  $k'_c$ .

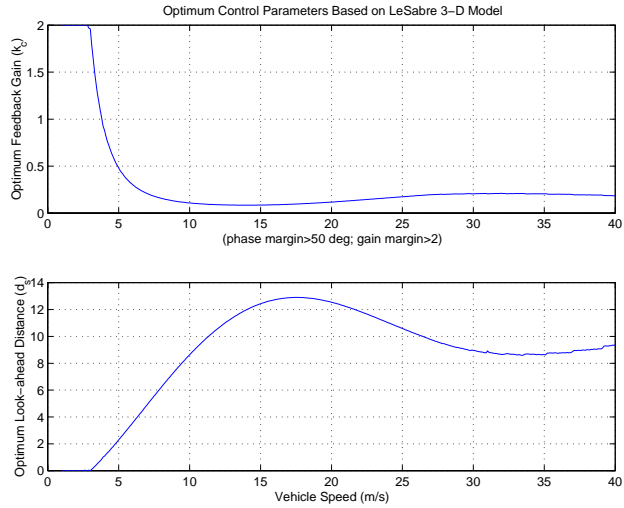


Figure 2.5.5 Optimal control gain pair  $(\bar{k}_c, \bar{d}_s)$  based on 3 DOF model with constant control parameters ( $pm=50$  deg,  $gm=2$ )

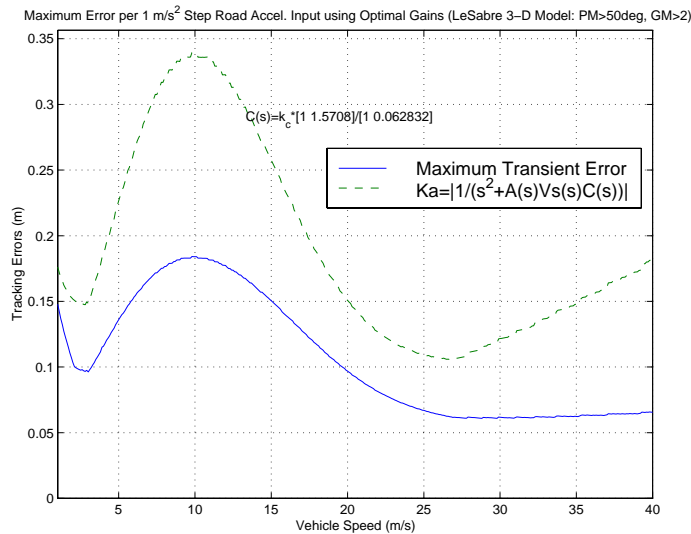


Figure 2.5.6 Resultant maximum transient error from the optimal control gain (in Figure 2.5.5) based on 3 DOF model with constant control parameters ( $pm=50$  deg,  $gm=2$ )

### C. Optimal Frequency-Shaped Look-ahead Steering Controller

The results in the previous section imply that a simple controller combining constant feedback gain and constant look-ahead distance may achieve all performance requirements described in Section 5.3.2 for both precision docking and other BRT operations. However several practical constraints limit the feasibility of such simple implementation. The amplification of the measurement noise limits the length of the look-ahead distance to a couple of car length; high feedback gain with large look-ahead distance can easily excite the non-linearity or unmodeled dynamics in the steering

actuators or mechanism; large look-ahead distance creates noticeable steady state tracking error during curves.

In order to address both the practical limitations and the specific phase lead requirement associated with the constant look-ahead distance depicted in Section 5.2.3.C, a frequency shaped look-ahead controller law is proposed as

$$V_s(s) = sG_{\delta}(s) + d_s(v)G_{ds}(s)sG_{\delta}(s) + h_s sG_{\delta}(s), \quad (2.20)$$

along with a feedback compensator

$$C(s) = k_c(v)G_c(s). \quad (2.21)$$

Following the design philosophy of minimum controller transition, two speed-independent filters,  $G_{ds}(s)$  and  $G_c(s)$ , are chosen for investigation in this section. In order to reduce both the effects of the steady state tracking bias and the unwanted excitation of the high frequency unmodeled dynamics,  $G_c(s)$  consists of a low-frequency integrator and high-frequency roll-off. Similarly,  $G_{ds}(s)$  is made of a high frequency roll-off portion and a mid-frequency lead-lag filter to limit the look-ahead amplification and to provide extra “look-ahead” between 0.5 and 2 Hz. In this section, these two additional control filters are chosen as

$$G_c(s) = \frac{25\pi(s + 0.5\pi)}{(s + 0.02\pi)(s + 25\pi)} \quad (2.22)$$

$$G_{ds}(s) = \frac{20\pi(s + 0.4\pi)}{(s + 0.8\pi)(s + 10\pi)} \quad (2.23)$$

Inserting  $G_{ds}(s)$  into  $V_s(s)$  as in Eq. (2.20) and appending  $G_c(s)$  to all open loop transfer function immediately after  $V_s(s)$  for Eqs. (2.14) to (2.17), the corresponding optimal control gain pair  $(\bar{k}_c(v), \bar{d}_s(v))$  that satisfies the stability requirements (2.7) and (2.8) for any given vehicle speed  $v$  is calculated as in Eq. (2.18).

The optimal control gain pair  $(\bar{k}_c(v), \bar{d}_s(v))$  corresponding to the control filters  $(G_c(s), G_{ds}(s))$ , as well as the resultant maximum transient error and error bound  $(K_a)$  are plotted in Figure 2.5.7 and 2.5.8. Similarly, the optimal gain pairs guarantee at least 50 degrees phase margin and 6 db gain margin for any vehicle speed. As the result of the additional phase lead created by the larger look-ahead distance between 0.5 and 3 Hz, the frequency-shaped look-ahead scheme renders a more desirable optimal gain pair characteristics. Generally speaking, the look-ahead distance increases and the feedback gain decreases as the vehicle speed increases. More specifically,  $(\bar{k}_c(v), \bar{d}_s(v))$  remain almost constant for vehicle speeds between 15 and 30 m/s. This indicates that a “constant” controller can work almost optimally from medium to highway speeds. Generally speaking, the relatively “flat” gains with respect to velocity imply that the controller is more tolerant to velocity errors.

Figure 2.5.8 shows that the resultant maximum tracking error (including transient) is less than 15 cm for every 0.1g lateral road disturbance without any prior knowledge of road curvature. It satisfies all lane-tracking requirements specified in Section 2.5.2 at any speed.

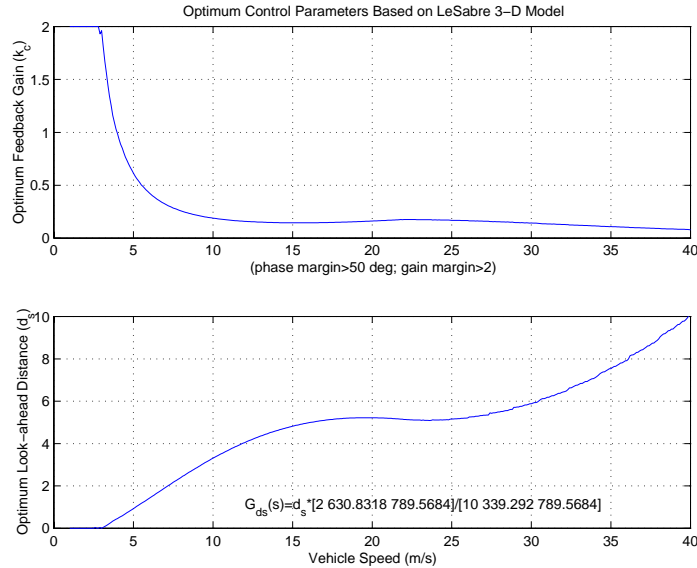


Figure 2.5.7. Optimal control gain pair ( $\bar{k}_c, \bar{d}_s$ ) based on 3 DOF model with frequency shaped look-ahead control ( $pm=50$  deg,  $gm=2$ )

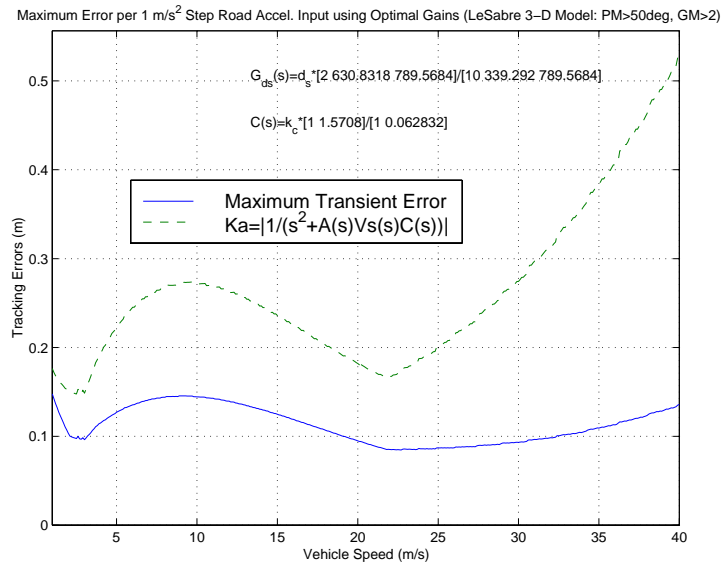


Figure 2.5.8. The resultant maximum transient error and  $K_a$  based on 3 DOF model with frequency shaped look-ahead control ( $pm=50$  deg,  $gm=2$ )

#### D. Final Controller Implementation

The above section provides strong arguments for implementing the frequency-shaped look-ahead steering controller in practice: simple, robust and satisfying performance requirements. Eq. (2.20) can be directly adopted for controller design when the yaw angle measurement is available. On the other hand, when the vehicle uses a “look-down” lateral sensing system for lateral control, the yaw angle can be estimated by a second “look-down” measurement. Under the assumption that the distances from all sensors to roll axis are about the same, the lateral displacement at a virtual look-ahead distance,  $d_s$ , in front of the CG can be easily approximated according to Eq. (2.3) as

$$y_s \cong y_f + (d_s - l_f) \frac{y_f - y_b}{L} \quad (2.24)$$

where  $y_f$  and  $y_b$  are the lateral measurements in front and back of the vehicle, respectively, and  $L$  is the distance between these two sensors.

The final steering control algorithm implemented in the test vehicle needs to satisfy both tracking accuracy and ride comfort requirements for all operational scenarios discussed in Section 2.5.2 at various vehicle speeds regardless of the following uncertainties: road adhesion variations, incorrect road curvature information, sensor noises, actuator bandwidth, vehicle dynamics changes, soft suspension modes, and vehicle parameters. Using the analysis results from this paper with some tuning in the vehicle, the following final frequency shaped virtual look-ahead lane-keeping control algorithm was developed and implemented:

$$\delta_c = -k_c G_c(s) \left( (k_{int}(s) + k_e G_{ds}(s)) y_f - k_e G_{ds}(s) y_b \right) \quad (2.25)$$

where  $\delta_c$  is the steering command,  $k_{int}$  the integrator at front sensor location,  $G_{ds}$  the virtual sensor look-ahead filter,  $G_c$  the compensator at the virtual sensor location,  $k_e$  and  $k_c$  are the gain-scheduled constants. Notice that  $k_e = (d_s - d_f) / L$ . These two gain-scheduled coefficients follow the velocity dependent relationships from Figure 2.5.7.

This final algorithm consists of three linear filters similar to those shown in Figure 2.5.9. These filters are basically slight variations of  $G_c$  and  $G_{ds}$  as described in the last section. Some small modifications were made through limited vehicle tuning to address “subjective” tradeoffs as well as certain identifiable unmodeled dynamics. These three filters and their primary functions are described as follows:

- An integral control,  $k_{int}(s)$ , that keeps the steady state tracking error at the front sensor to zero.
- A frequency shaped look-ahead distance,  $G_{ds}(s)$ , that provides more look-ahead distance around the vehicle lateral modes and roll-off of the look-ahead distance at higher frequencies.
- A servo controller,  $G_c(s)$ , that uses the frequency shaped virtual displacement as input and compensates it for the actuator and noises.

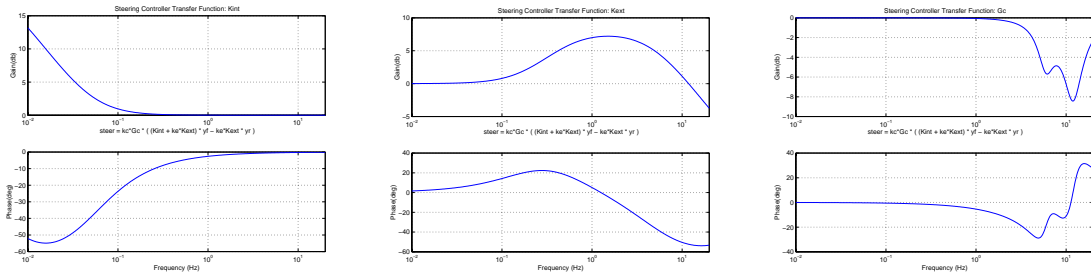


Figure 2.5.9. Final controller frequency responses  
(Left:  $k_{int}(s)$ , Center:  $G_{ds}(s)$ , Right:  $G_c(s)$ ).

## 2.6 Detailed Bus Precision Docking Software Structure

The section described the detailed Bus Precision Docking Software structure. The general structure is shown in figure 2.6.1.

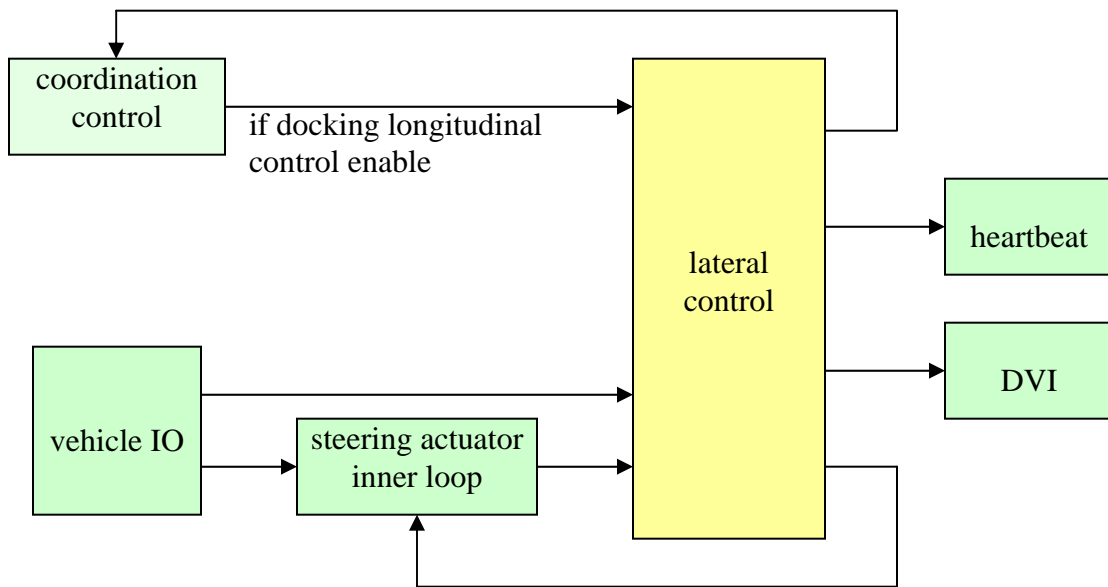


Figure 2.6.1 Bus precision docking software structure

The lateral control software gets a trigger from the magnetometers every 2 msec, and reads the following 8 structures from the database:

- magnetometers (DB\_LAT\_INPUT\_MAG)
  - lateral and vertical axis of front 7 sensors
  - lateral and vertical axis of rear 7 sensors
  - overall magnetometer health from the 14 sensors
- steering actuator inputs (DB\_LAT\_CONTROL\_INPUT)
  - steering angle at the tire (deg)
  - actuator ready (0=not ready, 1=ready)
  - actuator status (0>manual, 1=automatic)

- actuator fault mode (0=none, 1 to 7=fault)
- other lateral sensors (DB\_LAT\_INPUT\_SENSORS)
  - lateral acceleration
  - steering actuator switch (on or off)
  - transition toggle switch (manual, none or automatic)
  - transition enable switch (on or off)
  - longitudinal enable switch (on or off)
- vehicle speed (m/s) from the J1939 bus (DB\_J1939\_CCVS)
- current vehicle gear from J1939 bus (DB\_J1939\_ETC2)
- yaw rate (rad/sec) from the gyro (DB\_GYRO)
- DVI lateral mode from the buttons (DB\_DVI\_MONITOR)

In the docking longitudinal control enable, it also reads:

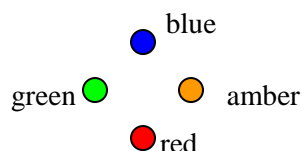
- longitudinal coordination inputs (DB\_LONG\_COORD\_OUTPUT)
  - longitudinal controller status (0=manual, 1=automatic)
  - longitudinal controller fault mode (0=none, 1=parking brake)
  - brake override (true or false)
  - brake switch (on or off)
  - throttle switch (on or off)

The lateral control software writes the 6 following structures to the database. Every 2 msec, it writes:

- lateral outputs for the steering actuator (DB\_LAT\_CONTROL\_OUTPUT)
  - steering actuator mode (0=manual, 1=automatic)
  - desired steering angle (deg)
- lateral coordination outputs for longitudinal control (DB\_LAT\_COORD\_OUTPUT)
  - command for the longitudinal controller (0=manual, 1=automatic)
  - command to resume longitudinal controller after stopping (true or false)
  - estimated longitudinal position of the bus from the magnets (m)
  - stop marker number for the next bus stop

And every 50 msec, it writes:

- computer heartbeat (DB\_LAT\_HEARTBEAT\_OUTPUT)
- DVI leds and sounds (DB\_DVI\_LEDS)
  - green led (on when transition to automatic is ready)
  - blue led (flashing when transitioning to automatic, on when in automatic control)
  - red led (on if lateral fault, flashing if emergency fault, off if no fault)
  - amber led (flashing if longitudinal fault, off if longitudinal control on)



- ready sound (on if lateral control is ready to engage)
- confirmation sound (on if driver pushes the transition switch)
- take over sound (on if end of magnets)
- emergency sound (on if emergency lateral fault)
- o DVI outputs to the monitor (DB\_LAT\_DVI\_OUTPUT)
  - overall mode of the lateral process for the docking scenario:
    - DOCK\_SELECT: select docking scenario
    - DOCK\_START\_WARNING: automatic transition is engaging
    - DOCK\_ACTIVE: automatic control on
    - DOCK\_FINISHED: docked, waiting at the bus stop
    - DOCK\_FROM\_PARKED: leaving bus stop
    - DOCK\_NOT\_IN\_DRIVE: docked, parking brake or not in gear fault
    - DOCK\_BRAKE\_ON\_ERR: driver hits the brake => longitudinal control is disabled and lateral control is still engaged
    - DOCK\_FAULT: fault code, lateral control is disabled
  - magnets read (true or false)
  - lateral system ready to transition (true or false)
  - automatic transition enable for docking (true or false)
  - station number for docking (0=none, 1=first station or 2=second station)
  - main lateral fault (0=none, 1&2= fault, -1 to -6=emergency fault)
  - additional fault for actuator and magnetometers (unused in the demo)
  - travel direction (0=unknown, 1=northbound or 2=southbound)
  - lane ID (0=unknown, 1=right or 2=left)
  - lane change direction (0=none, 1=right or 2=left)
  - lateral offset (cm)
  - estimated lateral measurement during lane change (cm)
  - remaining distance to the end of the magnets (m)
  - vehicle speed (4\*m/s)

### ***3. Fault/failure analysis, diagnosis and safety design considerations***

Safety is the most important consideration for any automated vehicle design. Safety issues include fault and failure analysis, diagnosis and safety designs. This section discusses the implemented fault detection system in the test vehicle, the bench safety analysis for the steering actuator, as well as other fault and failure analysis.

#### **3.1 Implemented Fault Detection Systems**

The fault detection and failure management systems are the crucial components in any automated vehicle systems. In the precision docking system designed under this project, we tried to include most of the crucial component failure detections in the implementation. However, the complexity of such design increases as the complexity of the failure scenarios increase. Due to the limited time and resources available for the project, the detection design may not be as comprehensive as it would required for field-



test ready automated buses. Furthermore, redundancy is not implemented for this test system for the same resource limitations. Again, we are aware of the fact that any possible single point failure should have redundancy to protect the system safety and integrity.

Two levels of fault detections are implemented for the test buses: component level fault detection and higher-level lateral control fault detection.

Two component-level fault detections are implemented. The magnetometer manufacturer designed hardware fault detection for each magnetometer, and PATH design software fault detection for the smart steering actuator.

Each magnetometer provides a digital health signal output to signify any detected failure in the magnetometer electronics.

The steering actuator motor provides also a “digital” failure output that indicates a hardware/electronic motor failure by the manufacturer. The smart steering actuator software designed by PATH includes local fault detection that addresses the following possible failure situations: motor failure detected by the motor electronics (motor failure), no power (power off), conflicting commands indicating host computer problems (command failure), steering actuator lower-level driver failure (driver failure), encoder inconsistency (encoder failure), steering pot inconsistency (steering pot failure), and initialization problem (start up failure). The following lists the corresponding fault code numbers:

- 0 = none
- 1 = motor failure
- 2 = power off
- 3 = command failure
- 4 = driver failure
- 5 = encoder failure
- 6 = steering pot failure
- 7 = start up failure

The implemented main lateral control fault can be somewhat self-explained by the following designed main lateral control fault code:

- 0 = no fault
- 1 = yaw rate
- 2 = actuator pot sensor
- -1 = missing magnets
- -2 = speed
- -3 = magnetometer health
- -4 = steering actuator
- -5 = timing
- -6 = multiple fault

The 0 fault code means no fault. “Positive” faults are generally not “fatal”. The more “negative” the fault number is, the more serious the implication of the fault would be. The fault detections are designed to incorporate the inputs from the lower-level component fault detection as well as higher-level logics to provide an more clear overall assessment for the system health. The fault code is used in various DVI control and lateral control state machines.

## 3.2 Bench Analysis: Fault Detection of Steering Actuator

Due to the time limitations and safety implications for experimenting failure analysis under an automated bus, a hardware in the loop (HIL) environment was created to study one of the major safe-critical component in the precision docking automated system: the steering actuator. The fault detection in a HIL simulation contains two major portions: the HIL simulation and the fault detection study. The hardware setup and algorithm implementation of the HIL simulation will be presented in section 3.2.1. The simulation hardware includes part of the real steering system, a real-time computer, a set of sensors, a steering actuator, and a reaction motor, all in a bench. The fault detection, described in Section 3.2.1, is model-based fault detection scheme that utilizes a minimum set of electric components and simple algorithms to determine faulty steering actuator before automation.

### 3.2.1 Basic Hardware Setup

Figures 3.2.1(a) and 3.2.1(b) show an HIL simulation setup. The essential hardware of the HIL simulation contains four parts: (1) real mechanical mechanisms, (2) actuators, (3) sensors, and (4) control and data transfer units. The steering wheel, steering actuator, shafts, torsion bar, and rack & pinion are in the same scale of typical passenger auto parts. The reaction motor is employed to mimic the original system from two major aspects: (1) the dynamics of the steering system and (2) external forces and disturbances from the tires. For example, the loads and disturbances include the inertia forces of the tires and the aligning torques resulted from tires during cornering. The assist torque is to simulate that generated by power steering in a vehicles. Torque sensors and position encoders are utilized for measurements and for simulations. For instance, encoder B determines the steering angle on tires. Incorporated with vehicle lateral dynamics, the angle can be used to generate the aligning torque during cornering. Deflections between the upper and the lower columns can be employed to produce assist torques, i.e.

$\tau_{assist} = f(\theta_A - \theta_B)$ . ECU is used to supply and control the current into the DC motors.

The I/O boards, AT-MIO-64E-3 and AT-AO-6, are used to read the measurements, to output the torque commands, and to communicate with the computer.

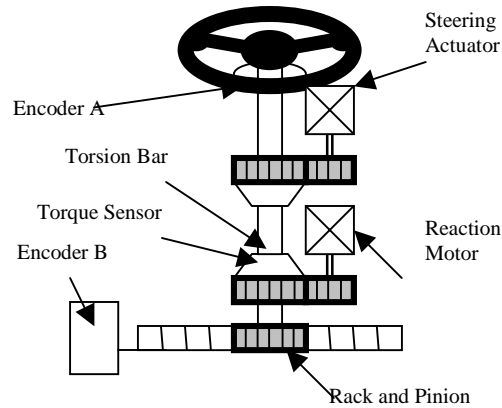


Figure 3.2.1(a) Overview of steering workbench

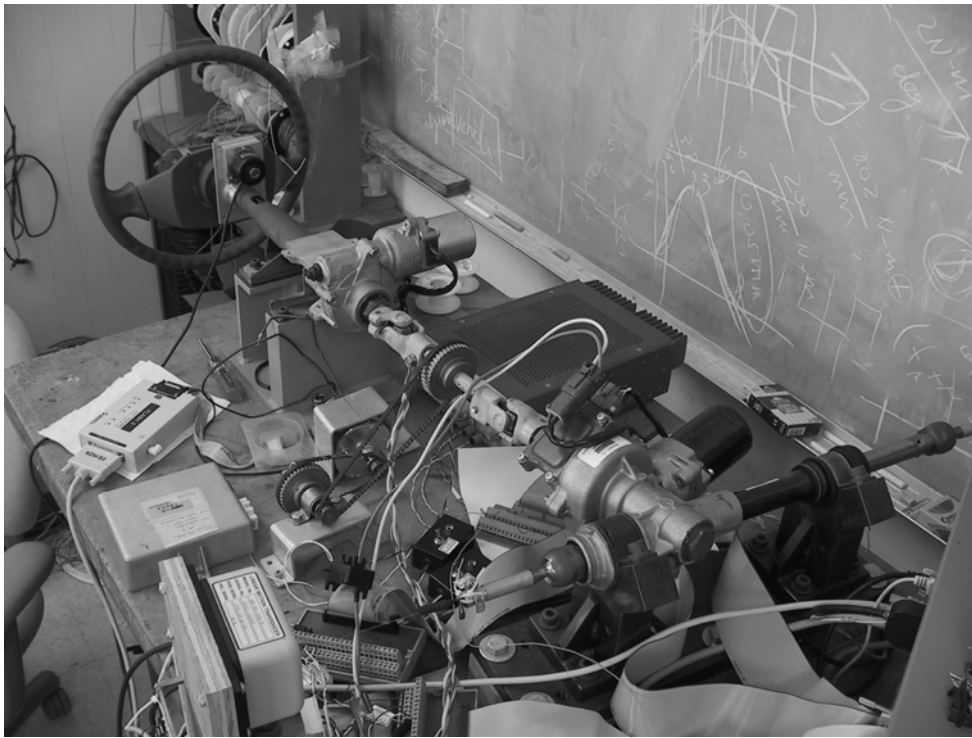


Figure 3.2.1(b) Steering workbench

### 3.2.2 Actuators

There are two motors acted as actuators used in the workbench: steering actuator and reaction actuator. The steering actuator is similar to those used in automated vehicles. The reaction actuator is added to simulate the actual reaction from the vehicle and the road as well as the characteristics of the steering system. Generally, the characteristics and reactions include the power assist steering, tire forces, loads, friction, damping, etc. These will be detailed in the following subsections. Table 3.1 shows the specifications of the two actuators. Note that the torque of the reaction motor is much larger than that of the steering actuator because, for example, the reaction motor may need to simulate the

large disturbances from the road in a sudden. This will require a large force at that time instant.

	Steering Column Actuator	Restoring Force Actuator
Gear type	Worm and worm gear	Worm and worm gear
Gear ratio	16.5 : 1	17 : 1
Motor type	DC brush motor with clutch	DC brush motor
Rated voltage	DC 12V	DC 12V
Rated current	25 A	30 A
Rated motor speed	1250 rpm	1050 rpm
Rated torque	1.05 Nm	1.61 Nm
Rated output	135 W	170W
Torque constant	0.042 Nm/A	0.054Nm/A
Motor inertia	0.16 g-m <sup>2</sup>	0.24 g-m <sup>2</sup>

Table 3.1 Comparison between steering and reaction motors

### 3.2.3 Model Considerations

#### ■ Power Assist Steering

Figure 3.2.2 shows a typical characteristic curve of the assist torque versus deflection on the torsion bar. The slope of this curve rises up as the deflection increases. The more the driver's effort is, the larger the deflection on the torsion bar will be. The ratio between the applied torque of the driver and the assist torque will then become smaller. The assist torque will generally "compensates" the external loads and disturbances at large deflections while human driver's hand will compensate such forces at small deflections.

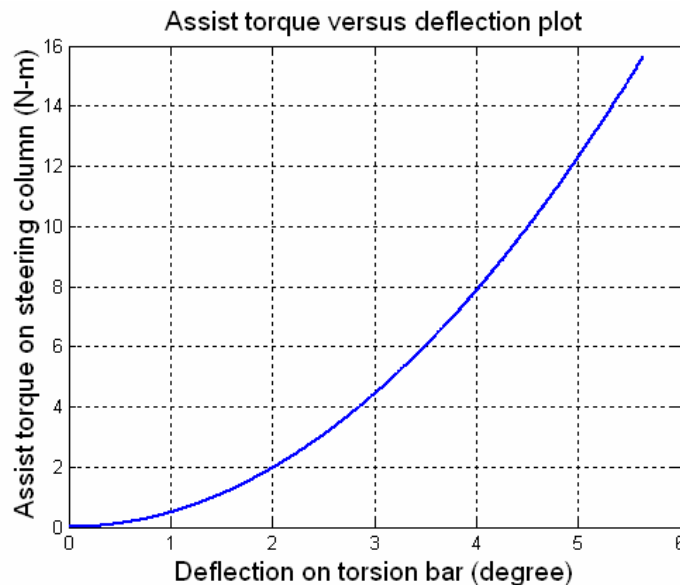


Figure 3.2.2 Assist torque versus deflection of torsion bar plot

## ■ Self-aligning Torque

Aligning torque describes a tire's tendency to steer about a vertical axis through the "center" of the print (the origin of the tire axis system). Usually the tire tends to align its heading with its path. The aligning torque comes from the shape of the distortion in the footprint. The elastic distortion increases from front to back and this gives an uneven distribution of lateral force along the length of the print. Figure 3.2.3 shows the deflections of the tire contact patch in a simplified tire model. Given foundation stiffness,  $c$ , and small deformations, the concentrated force is approximately  $\frac{1}{2}cl^2\alpha$  while the moment along the vertical direction is  $\frac{1}{12}cl^3\alpha$ , where  $\alpha$  is the slip angle. In *elastic* region, the moment will be increasing proportionally with  $\alpha$  since the moment is independent of  $c$  and  $l$ .

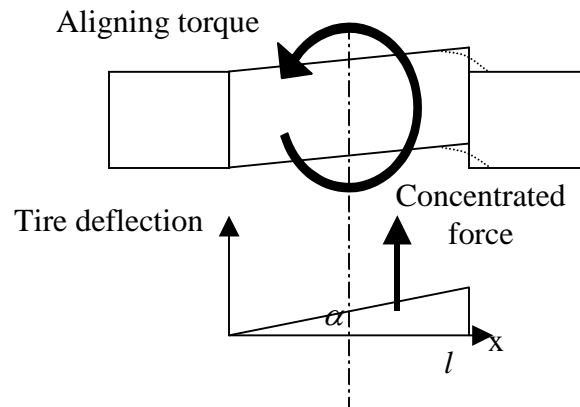


Figure 3.2.3 Tire treads deflection in elastic region

As the rear of the tread in the footprint slides, the local deformation in the sliding region reaches the limit, shown in figure 3.2.4. First, the total lateral force still increases but it is not as much as that generated by using linear tire model at the same slip angle. Secondly, the concentrated force will move forward, closer to the tire center. Due to the above two effects, the moment may reach the peak value in the *transitional* region, as shown in figure 3.2.5.

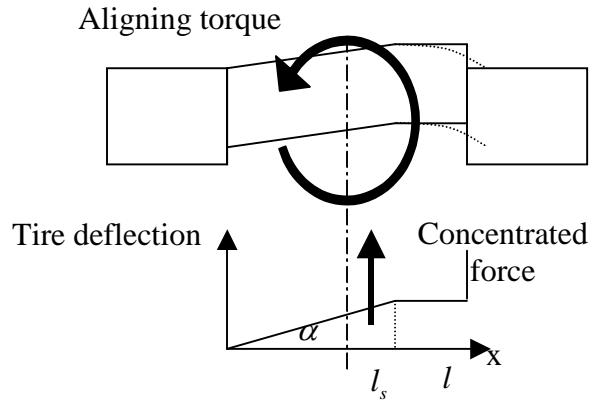


Figure 3.2.4 Tire treads deflection in transitional region

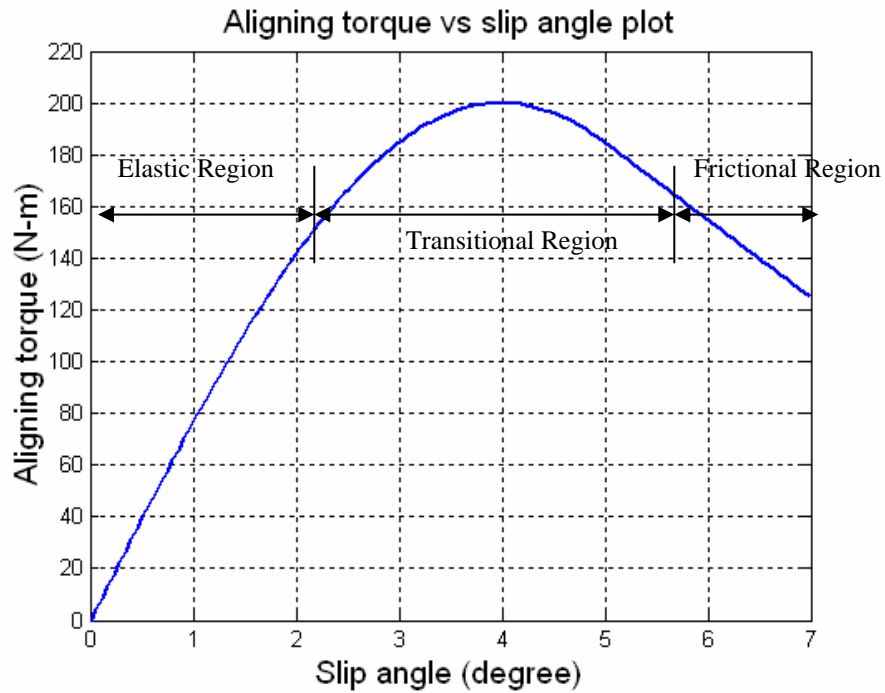


Figure 3.2.5 Aligning torque versus slip angle plot

Once the total lateral force reaches the maximum value, it is often referred to as the *frictional* region. In this region, as the slip angle goes up, the resultant lateral force will be focused much closer to the center of the tire and the moment will continue falling off.

At this stage, the aligning torque is discussed based on the viewpoint of the tire itself. From the aspect of the whole system, this torque is not equivalent to that applied to the steering mechanism. The aligning torque will be amplified or reduced because of introducing steering geometry, such as castor, camber, and inclination angles. In many designs of automotive steering systems, these angles are used for better vehicle lateral characteristics. The steering geometry has to be taken into consideration when implementing HIL simulation. For example, Figure 3.2.6 shows kingpin offset due to the

effect of castor angle. The mechanical trail represents for the kingpin offset while the pneumatic trail results from the uneven distribution of the lateral forces. The steer torque is given by the sum of mechanical trail plus pneumatic trail times the lateral force. This will assist human drivers in faster steering wheel aligning, especially at low speeds.

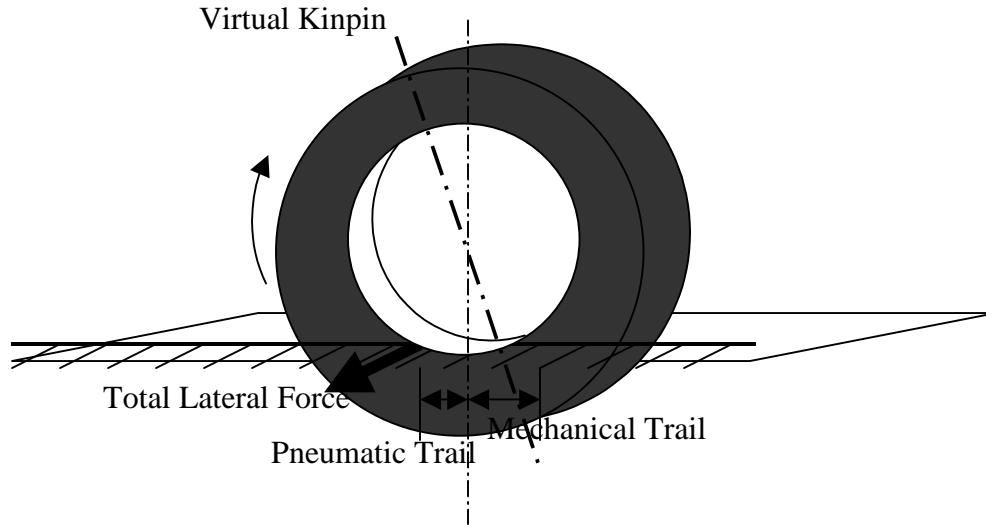


Figure 3.2.6 Castor angle effect on aligning torque

The aligning torque depends on the steering geometry and the slip angles of the front tires. Slip angles are determined based on the interactions among the ground, the vehicle, and the tires. In the HIL simulation, the interactions have to be simulated by using computer programs. In this study, a bicycle model with nonlinear tire characteristics has been utilized to calculate the slip angles at each time instant. The equations of motion of a bicycle model are shown as follows.

$$m\ddot{y}_u = F_f(\alpha_f) + F_r(\alpha_r) \quad (3.1)$$

$$I_{zz}\ddot{\psi} = F_f(\alpha_f)l_1 - F_r(\alpha_r)l_2 \quad (3.2)$$

where  $m$ : vehicle mass

$I_{zz}$ : moment inertia of yaw motion

$\alpha$ : slip angle

$l_{1,2}$ : distance between C.G. and front/rear axle

$F_i$ : lateral force at front/rear axle.

### ■ Friction, Damping, and Inertia Forces

In the real steering system, there are large friction and damping forces from the tire-ground interface, rack & pinion, joints, tire intrinsic properties, etc. The real system has large loads, such as the wheel inertia. However, in the workbench setup the simulated system only contains part of the real hardware. To mimic the actual system, these forces have to be included during the simulation.

### 3.2.4 Implementation of HIL Simulation

The effects mentioned in section 3.2.3 should be included to simulate the major characteristics of the vehicle steering system. Most of the above effects are simulated using the reaction motor. Ideally, the workbench can perfectly mimic the real system if the motor does not have its own dynamics. However, it is not true in the real world. The motor dynamics may result in some problems that the real steering system does not have. In fact, there is a stability problem in implementing the assist torque.

The stability problem arises after adding the large assist gain into the simulation. From the perspective of the reaction motor, its ECU receives the commands of the aligning torque and the assist torque to drive the system from the lower column. The magnitude of the assist torque depends on the deflection between the upper and the lower columns. Figure 3.2.7 shows the block diagram of the simplified workbench model. In this diagram, the input is the torque command and the output is the deflection of the torsion bar.

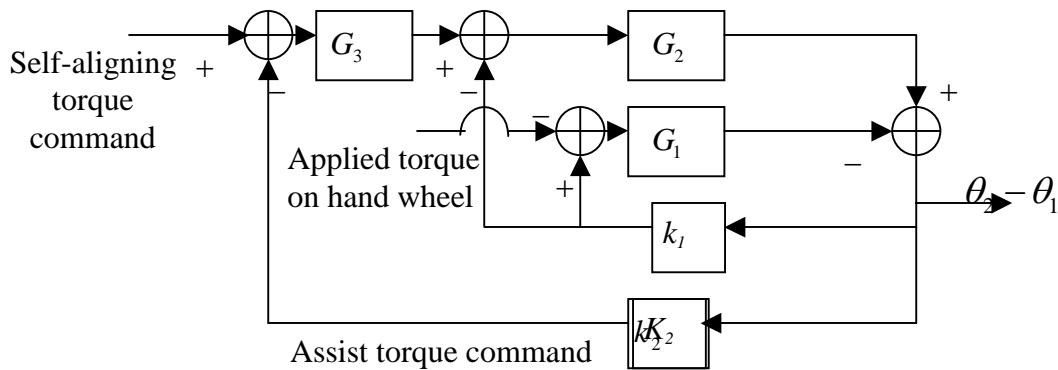


Figure 3.2.7 Block diagram of simplified steering system

where  $G_1$  and  $G_2$  are the transfer functions (from  $\tau_i$  to  $\theta_i$ ) of upper/lower steering column  
 $G_3$  is the transfer function of ECU with reaction motor dynamics  
 $\theta_1$  and  $\theta_2$  represent the angular displacement of upper/lower steering column  
 $k_1$  is the spring constant of the torsion bar  
and  $k_2$  is the gain of the assist torque.

If the motor dynamics is ignored, say  $G_3$  equal to unity, the overall closed loop transfer function from the motor command to  $\theta_2 - \theta_1$  is  $\frac{G_2}{1 + k_1(G_1 + G_2) + k_2G_2}$ , where  $G_1$  and  $G_2$  are stable 2<sup>nd</sup> order systems with relative degree 2. The Nyquist plot of  $k_1(G_1 + G_2) + k_2G_2$  will never enclose  $-1$  for any positive assist gain,  $k_2$ , since the phase of  $G_1$  and  $G_2$  can only vary from 0 to  $-180$  degrees. After the motor dynamics,  $G_3$ , is introduced into the system, the closed-loop transfer function will



become  $\frac{G_2 G_3}{1 + k_1(G_1 + G_2) + k_2 G_2 G_3}$ . Because the dual-mass spring system is slightly damped,  $k_1(G_1 + G_2)$  can be very close to  $-1$  with little phase margin. Assume that  $G_3$  has relative degree of 1<sup>1</sup> and is a stable, minimum-phase transfer function. If the bandwidth of  $G_3$  is not much higher than that of  $k_2 G_2$ , the resultant vector,  $k_1(G_1 + G_2) + k_2 G_2 G_3$ , can be on the left hand side of  $-1$  at some frequency, as shown in figure 3.2.8. This implies that the Nyquist plot will enclose  $-1$  and will lead to an unstable system.

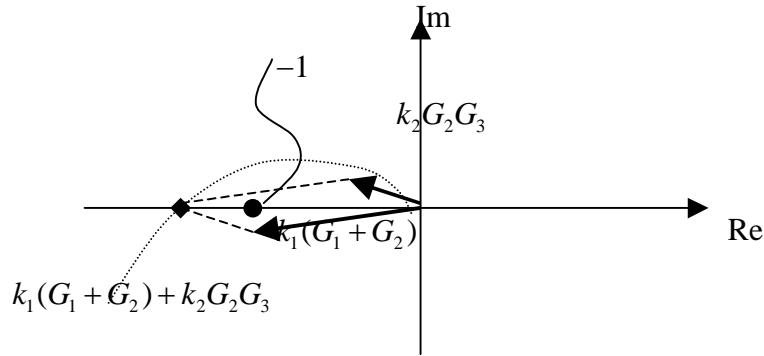


Figure 3.2.8 Nyquist plot of  $k_1(G_1 + G_2) + k_2 G_2 G_3$

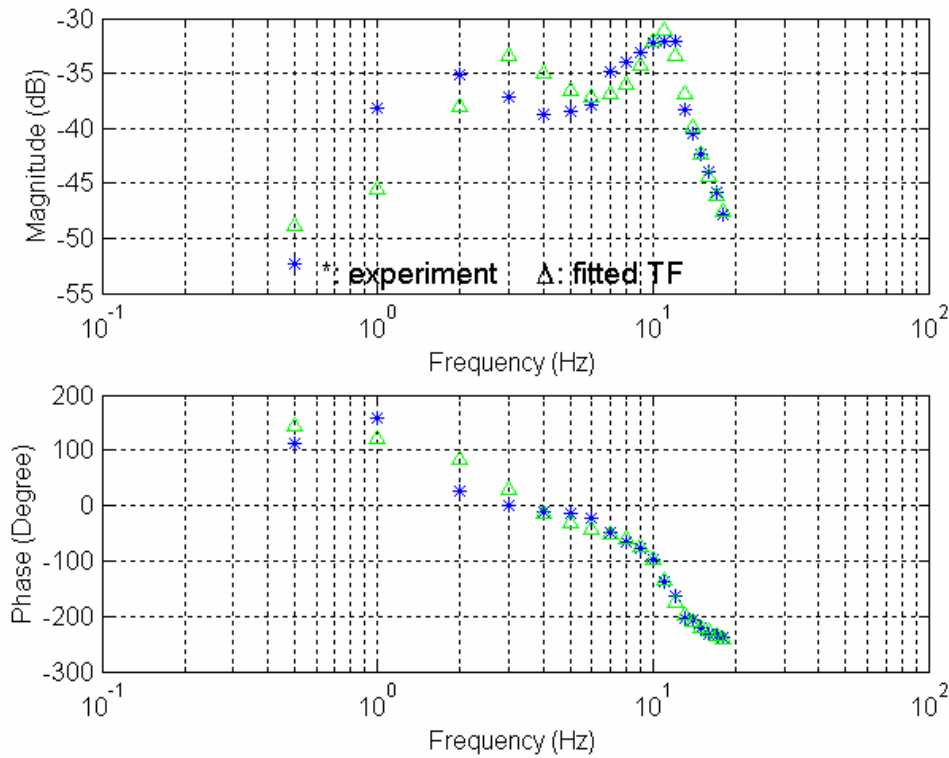


Figure 3.2.9 Bode plot from motor command to  $\theta_2 - \theta_1$

<sup>1</sup> The bandwidth of the actuator's LR circuit is over 100 Hz. The dynamics is ignored in the discussion.

By using the frequency sweeping technique, the identified Bode plot is shown in figure 3.2.9. In the diagram, it shows that the natural frequency of the mass-spring system is around 11 Hz and the phase is approaching  $-270$  degree at high frequency. The open-loop

transfer function from torque command to  $\theta_2 - \theta_1$  is  $\frac{G_2 G_3}{1 + k_1(G_1 + G_2)}$ . Based on the

assumptions made in the previous paragraph, this implies that the relative degree of the open-loop transfer function is 3, which follows the identified results. Therefore a pre-compensator has been specifically designed to stabilize the “inner loop” for the high assist gain. This presents another difference between the real hydraulic assist behavior and the one in the HIL simulation. However the difference, hopefully, only shows up in the higher frequency dynamics, which is not a concern for this study.

### 3.2.5 Model-based Fault Detection

The HIL simulation is eventually employed to study the fault detection of the steering actuator. This study focuses on model-based fault detection and identification. Fault identification is conducted by comparing the identified faulty system with a model of the fault free system. In this section, the actuator fault detection includes the two parts: (1) the basic knowledge of the motor dynamics and its control unit; (2) the fault detection algorithm, as presented in section 3.2.5.1 and 3.2.5.2, respectively.

#### 3.2.5.1 Basic Knowledge of Motor Dynamics and ECU

Figure 3.2.10 shows the DC motor dynamics. There is a first-order dynamics between the current and the effective voltage applied to the motor circuit. The torque generated is proportional to the current by the torque constant,  $K_t$ . The induced voltage will decrease the effective voltage applied to the motor circuit. An intuitive idea to follow the current command is that ECU can increase its output voltage to compensate for the back emf and reduce the phase lag resulted from the motor dynamics by utilizing the information from the built-in voltage and current sensors.

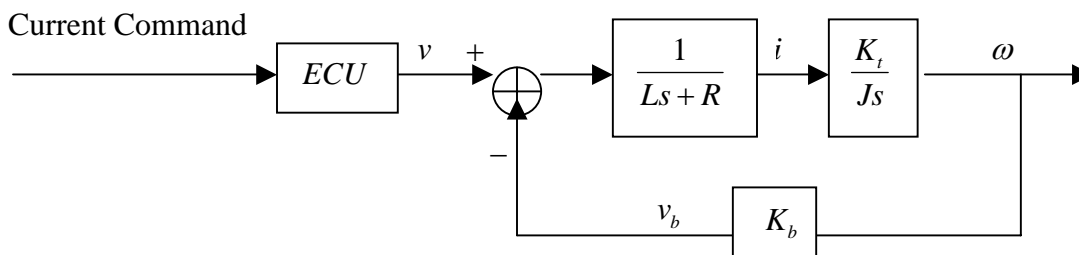


Figure 3.2.10: Block diagram of motor dynamics  
 $K_t$ : torque constant;  $K_b$ : back emf constant;  $J$ : moment of inertia

In summary, there are two voltage sources: (1) the applied voltage from the ECU; (2) the induced back electromotive force (*back emf*) from the motor. Usually the voltage applied to the motor is in pulse width modulation (PWM). This PWM signal can reach up to 50 kHz in some applications. Feeding into the circuits, the motor presents an inductive load and its inductance filters much of the high-frequency energy. The current will rise up as PWM signal is on and fall off as the PWM is off. The result is that the current looks like a DC signal with some ripples on it, as shown in figure 3.2.11. So the low frequency signal in the PWM can be measured by using the low pass circuitry with large impedance. From Faraday's law, the back emf will be induced against the armature voltage as the rotor windings spinning in the magnetic field. Ideally, if the two voltages are examined individually, the fault in the motor or in the ECU can be identified.

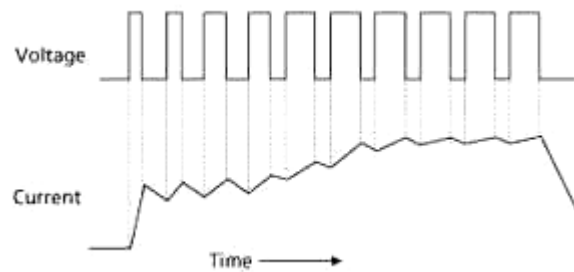


Figure 3.2.11 Current in PWM motors resembles DC with ripple (a motor's inductance filters high-frequency energy from the PWM drive voltage)

Since the ECU is often used to perform the current control, it will have incorrect responses if the fault exists in either the motor or the ECU itself. Either fault will lead to the failure of the automated steering system. For example, if the steering wheel is turned by human drivers, there will be emf produced from the motor accordingly. To keep zero current through the motor circuit, the ECU has to take some reactions. Failed or incorrect response implies the malfunctioned motor/ECU. Figure 3.2.12 illustrates this idea.

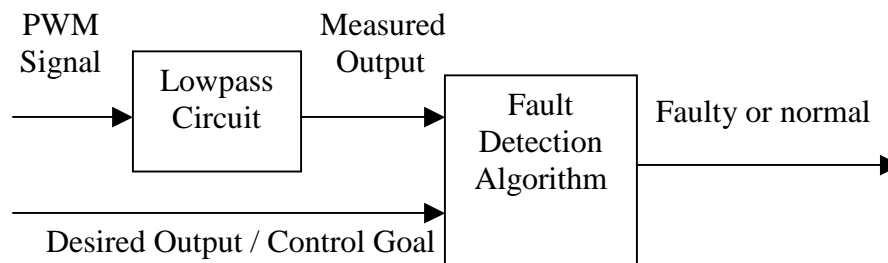


Figure 3.2.12 Schematic of fault detection

### 3.2.5.2 Fault Detection Algorithm

Figure 3.2.13 shows the comparison between the measured response from the steering actuator's ECU and the angular speed of the motor times the nominal back emf constant. This was performed under the large torque sinusoidal input at 9 Hz by utilizing the

reaction motor. As can be seen, the voltage generated from the ECU follows the desired signal well. This implies the estimated back emf constant,  $\hat{K}_b$ , is approximately equal to the nominal value,  $\bar{K}_b$ .

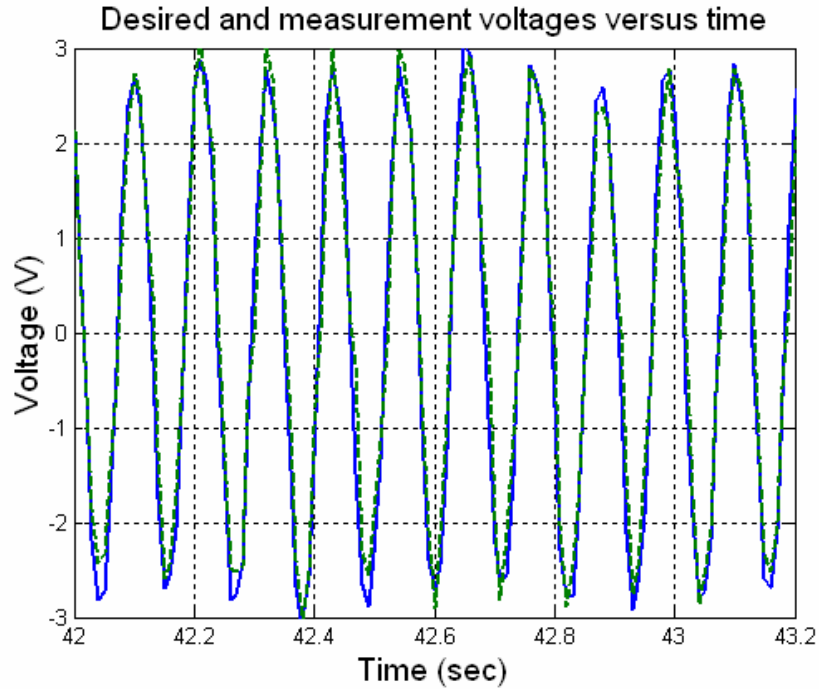


Figure 3.2.13 Voltage and Time (the solid line represents for the desired voltage based on the model and the dash line stands for the actual output from ECU)

However, in most situations on highways the angular speed of the steering wheel is small. As the signal is small, the noises, the disturbances, and the unmodeled dynamics may contaminate the measured signals significantly. Figure 3.2.14 sketches the desired and the measured signals under the small-input situation. It is difficult to estimate the back emf constant,  $\hat{K}_b$ , due to the low signal-to-noise ratio.

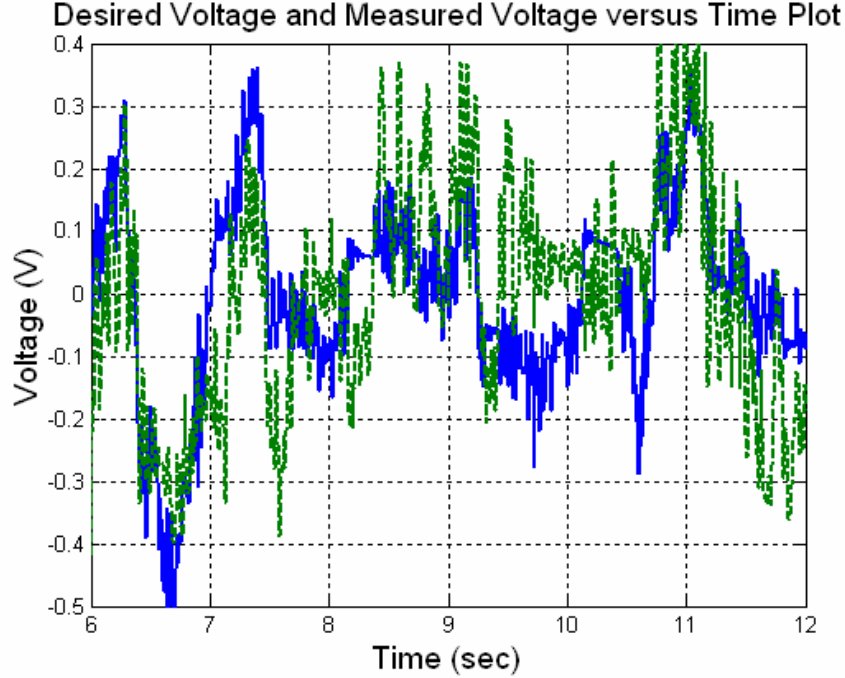


Figure 3.2.14 Voltage and Time (the solid line represents for the desired voltage based on the model; the dash line stands for the measured output from ECU)

In this study, a least square algorithm is employed to perform the fault identification task. The least square algorithm is a simple and robust approach. There are two reasons for the popularity of the least square estimation theory. The first reason is the ease of computation. The second is the desirable theoretical property of being the best linear unbiased estimation. Consider the following statistical model:

$$v_i^m = \theta v_i^d + e_i \quad (3.3)$$

where  $v_i^d$  and  $v_i^m$  are the desired and measured voltages, respectively,  $e_i$  is the noise, and  $\theta$  is defined to be unity if the system is normal. By minimizing the cost function,  $J(\theta) = \|v^m - \theta v^d\|^2$ , the estimation of  $\theta$  is shown in the following manner:

$$\hat{\theta}_{LS} = (v^{d*} v^d)^{-1} v^{d*} v^m = \frac{\sum_i v_i^d v_i^m}{\sum_i (v_i^d)^2} @ \frac{\hat{K}_b}{K_b^{true}} \quad (3.4)$$

The estimated back emf constant,  $\hat{K}_b$ , is determined given the data in the past. As shown in figures 3.2.13 and 3.2.14, the large input has good S/N ratio and, conversely, the small input has poor S/N ratio. Intuitively, it can be inferred that the larger the input signal is, the fewer the data points are needed for the desired accuracy of the estimator. This idea can be further elaborated as follows. Eq. 3.3 can be rewritten in matrix notation:

$$v_{o_z} = v_{o_z} \theta^{true} + e_{o_z}, \text{ where } e_{o_z} \sim N(0, I). \quad (3.5)$$

$$E[\hat{\theta}_{LS} - \theta^{true}] = E\left[\frac{v_d^T (v_d \theta^{true} + e)}{v_d^T v_d} - \theta^{true}\right] = 0. \quad (3.6)$$

$$E[(\hat{\theta}_{LS} - \theta^{true})^2] = E\left[\left(\frac{v_d^T (v_d \theta^{true} + e)}{v_d^T v_d} - \theta^{true}\right)^2\right] = E\left[\frac{v_d^T e e^T v_d}{(v_d^T v_d)^2}\right] = \frac{1}{v_d^T v_d}. \quad (3.7)$$

Eq. 3.6 shows that the least square estimate is *unbiased* and Eq. 3.7 indicates that the algorithm is *consistent*. By definition, “*consistent*” means that the variance will approach zero as the length of the data goes to infinity. It implies that the least square estimate will converge to the true value with probability 1 if the length of the sequence is large enough. The estimation accuracy with a certain confidence can be achieved by setting the corresponding variances. Small signals need more samples than large signals to reach the same variance, i.e. accuracy. Hence, a variable time window can be employed to conduct the task.

As for making decision, it is often difficult to set a single threshold to identify the system status as “faulty” or “healthy”. Single threshold will easily lead to the problems of false alarms or missed detections. Let’s suppose that figure 3.2.15 shows the probability density functions of the estimated system parameters of the normal and faulty motors. Given the two special cases that the mean values of the actual system parameters are 25%  $K_b^{true}$  and 100%  $K_b^{true}$ , respectively, it is easy to distinguish the motor status by setting a single threshold since the density functions do not overlap. What if a faulty motor with a mean of the system parameter, 80%  $K_b^{true}$ , is also included in the model set? The single threshold will fail in most cases. This example shows that the difficulties lie on three things: (1) the estimated parameter represents the “noisy version” of the true value; (2) using single threshold will easily cause false alarms and missed detections; (3) the faulty condition of the motor/ECU has to be clearly defined. Particularly, how can the two motors, with the true parameters, 99.5%  $K_b^{true}$  and 100%  $K_b^{true}$ , be distinguished? It implies that there will be some grey areas under which it is not easy to determine the fault.

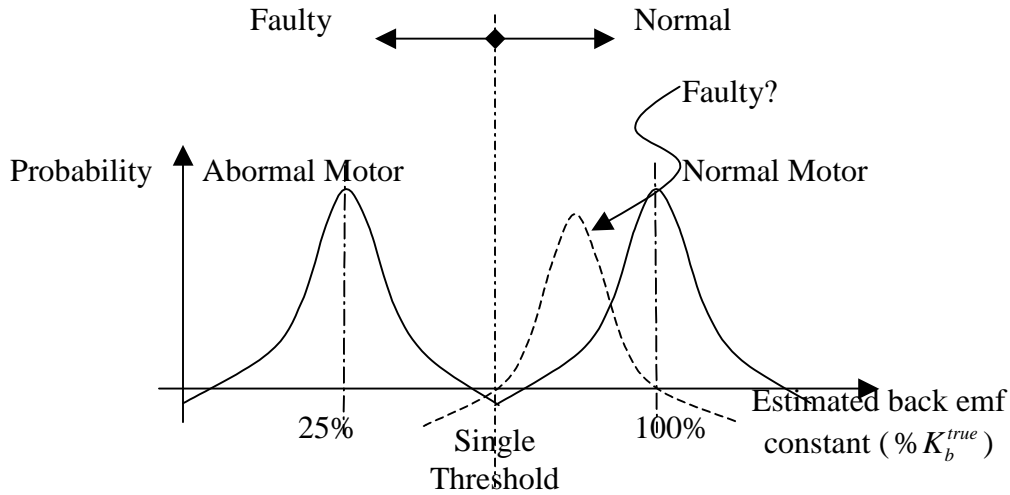


Figure 3.2.15 probability distribution of normal and faulty motors' system parameter

Introducing some intermediate states and basic rules can help determine the system fault. For example, the fault diagnosis can be conducted by using the criteria in figure 3.2.16.

{	$fault\_flag = 0$ (Healthy)	□	if $m_3 > r \geq m_4$
	$fault\_flag = 1$ (Not yet determined)	▒	if $m_4 > r \geq m_5$ or $m_2 > r \geq m_3$
	$fault\_flag = 2$ (Probably Faulty)	▓	if $m_5 > r \geq m_6$ or $m_1 > r \geq m_2$
	$fault\_flag = 3$ (Faulty)	■	if $r < m_6$ or $r > m_1$
, where $m_1 > m_2 > m_3 > 1 > m_4 > m_5 > m_6 > 0$		$m_1, m_2, m_3, m_4, m_5, m_6 \in \mathbb{R}$	

$r$  is the ratio between  $\hat{K}_b$  and  $\bar{K}_b$ .

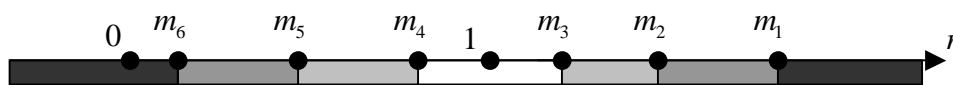


Figure 3.2.16 criterion of the system diagnosis

Figure 3.2.17 shows the experimental results of a normal motor/ECU combination. Before the first estimation result comes out, the estimate is set to one. The steering input starts at 6 sec and the first identified result shows up at 10.5 sec. The first result is delayed by 5.5 sec because the magnitude of the input is very small, 0.5 Volts peak to peak, and a wider time window has to be used to collect data. Between 10.5 and 12 sec, the fault flag shows “not-yet-determined” since the magnitude of the measured voltage, dotted line, far exceeds the desired voltage, solid line, from 8 to 10.5 sec.

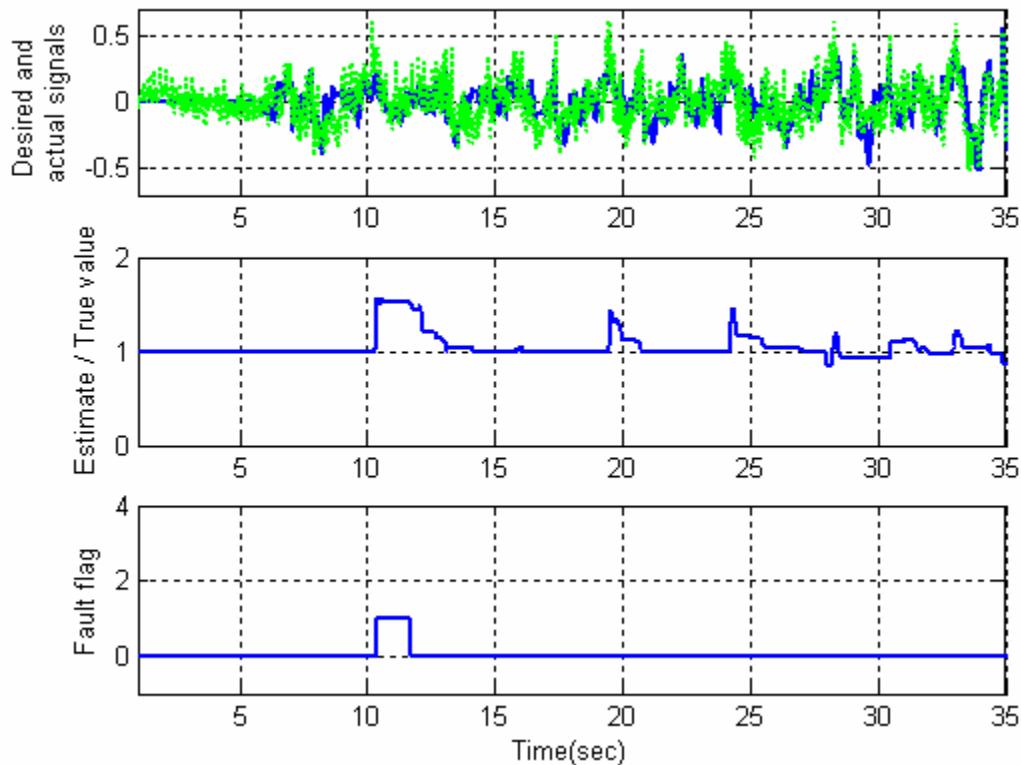


Figure 3.2.17 Motor/ECU in healthy condition

Figure 3.2.18 shows the identified results in a fault scenario. In this HIL simulation, the true back emf constant is set to be 40% of nominal value. The estimated parameter ranges from 0.1 to 0.7. By using the criterion shown in Figure 3.2.16, the fault flag does not show “faulty” all the times. It also stays in “probably faulty” and “not yet determined” sometimes. In fact, at this stage the decision-making only incorporates the criterion in Figure 3.2.16. If some rules can be introduced in the decision-making, the probability of false alarm and miss detection will greatly decrease.

The basic rules are concluded as follows:

- I. Vehicle automation is allowed if the system status remains normal within a certain time period.
- II. If the system stays in the “probably-faulty” status for a long time and the power of the desired signal exceeds some value, the condition will turn out to be “faulty”.
- III. If the status is “not-yet-determined” for some time and if the signal power in the time window is larger than a certain quantity, it will be set to “probably-faulty”.
- IV. If the system status falls into “faulty”, the system will be identified as “faulty” and a warning signal must be given.



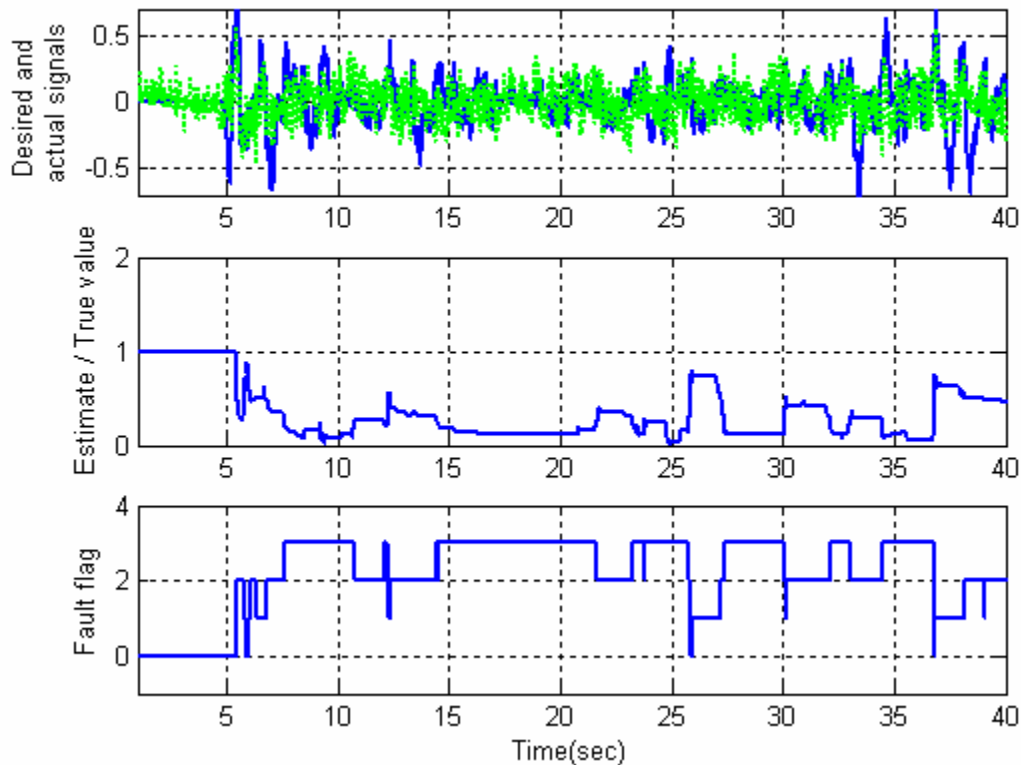


Figure 3.2.18 Motor/ECU in faulty condition

### 3.2.6 Conclusion

A hardware-in-the-loop simulation has been developed for studying the fault detection of the steering actuator. The simulation mimics most road-vehicle interactions and system reactions through the steering mechanism. The detection is model-based, utilizing onboard sensors to collect input and output datum. The least square algorithm is utilized to perform the system identification task. The multiple-threshold method incorporated with the basic rules can be used to determine the fault with the least possibility of false alarms.

## 4. Demonstration of precision docking system

Two demonstrations have been performed with the 40 ft bus: the first one at Washington DC on June, the second one is at San Diego on August.

### 4.1 Precision Docking scenario in Washington DC

Precision docking demo scenario in Washington DC is shown in Fig. 4.1. Bus starts at the beginning of the docking curve driven manually. During the straight-line segment,

transition to automatic control mode is initiated. The transition could be initiated by driver or by “automated transitioning”. Automatic control mode could be lateral (steering) control only or both lateral control and longitudinal control depending on driver selection. Once transition to the automatic mode, bus will steer itself along the predetermined magnetic track. If longitudinal automatic mode is selected, bus will accelerate and decelerate to about 10mph and cruise at this speed. Before stopping at the bus station, bus will make a full lane change follows the magnetic track. If longitudinal automatic mode is activated, bus will stop at docking station automatically. Otherwise driver should control bus longitudinally to stop at the docking station. Due to time constraint of demo preparation, the docking station in Washington DC demo is only placed at the bus’s front door.

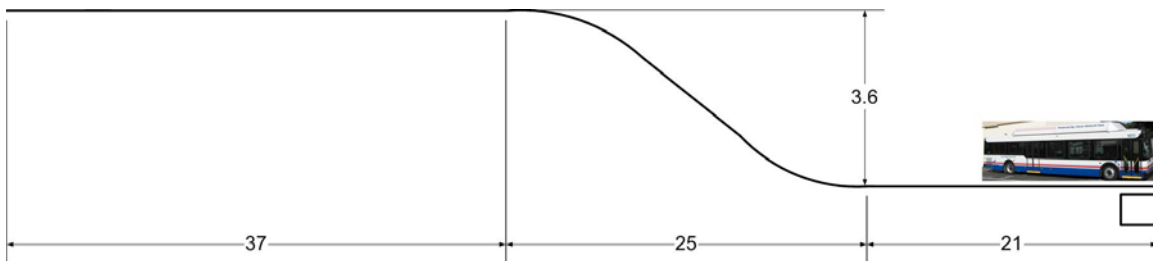


Figure 4.1 Precision Docking Demo Scenario in Washington DC (meter)

## 4.2 Precision Docking scenario in San Diego

Precision docking demo scenario in San Diego is shown in Figure 4.2. Bus starts at the beginning of the docking curve manually. During the straight-line segment, transition to automatic control mode is initiated. The transition could be initiated by driver or by control system itself. Automatic control mode could be lateral (steering) control only or both lateral control and longitudinal control depending on driver selection. Once transition to the automatic mode, bus will steer itself along the predetermined magnetic track. If longitudinal automatic mode is also selected, bus will accelerate or decelerate to about 10mph and cruise at this speed. Bus will first dock at the inline docking station. If longitudinal automatic mode is activated, bus will stop at inline docking station automatically. Otherwise driver should control bus longitudinally to stop at the inline docking station. After unloading and boarding, driver has two options to pull bus out of inline docking station. First, driver could steer bus manually out of inline docking station. Second, driver could just push the automatic button and control system will steer bus out of inline docking station automatically without driver interference. The rest of demo is similar to the Washington DC demo once bus moves out of inline docking station. Note that, the docking stations in San Diego demo is much longer than the docking station of Washington DC demo, both inline docking station and S curve docking station cover front door and rear door of the bus.

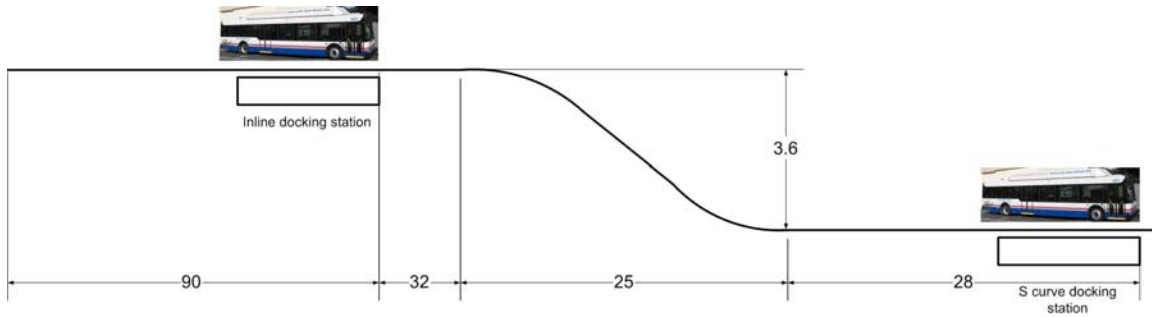


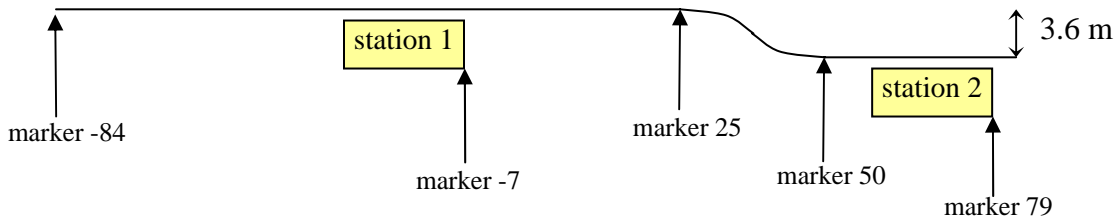
Figure 4.2 Precision Docking Demo Scenario in San Diego (meter)

On the San Diego test scenarios, the lateral control software can be used for two different scenarios:

- fully automated or lateral control precision docking
- fully automated or lateral control driving in the platoon on the HOV lanes

The overall software structure and the controller is the same. When the site is set to the South Control Yard (SCY), docking is chosen. When the site is set to I-15, platooning or lane assist/lane change is chosen.

For the San Diego docking track, magnets are installed every 1 meter as follows:



The first station is an in-line docking; the second station is an S-curve with a width of 3.6 m. Four codes of 6 bit each were installed, two for the first station and two for the second station.

## 5. Testing Results

Three categories of test results are shown in this section:

- Initial docking preparation results at Richmond Field Station
- Docking Demonstration results at Washington DC
- Dock test results at the South Control Yard at San Diego

### 5.1 Precision Docking Preparation at RFS

Figures 5.1.1 to 5.1.4 illustrate 26 consecutive precision docking preparation runs for the C2 40-ft bus at the Richmond station docking test track. Those were the initial runs when

the system was first successfully tested. The test track is basically the same as the one described above for the Washington DC demo except that the track is about 30 meter longer. Driver transition to automated control by pushing the “Auto” button in all of the test runs. More than half of the runs were conducted without automated longitudinal control. Figure 5.1.1 shows the time traces of all the runs. By observing the speed variations, it is clear that the driver controlled the throttle and brake for most of the runs. At one of the runs, the driver has slowed down the bus to almost stop and go situation.

Figure 5.1.2 illustrates the same plots as those in Figure 5.1.2 except that the data were plotted against marker numbers. Plotting against the marker numbers normalizes the data so that they can be compared at the every marker location for consistency and easy variations. These plots indicate clearly that the tracking repeatability is very high, to within couple of centimeters, once the bus enters the lane-change curve. On the other hand, the steering command had variance of more than 50 degrees. This further confirmed the design intuition that a high gain controller is essential for precision docking applications since a control method based on an “open-loop” type command would not produce consistent precision docking as indicated by Figure 5.3.2.

Figure 5.1.3 shows the blow-up plot of Figure 5.1.2 around the docking station. The blow-up plots clearly show that the bus has never touch the station, and the maximum error after bus is approaching the station is basically within 2.5 centimeter peak-to-peak.

Figure 5.1.4 exhibits the status of (1) the transitional switch (-1: none, 0: manual, and 1: auto), (2) the transitional status (0: manual, 1: automated), and (3) the control status (0: manual, 1: lateral control only, 2: lateral and longitudinal controls). It can be seen that the docking performance is highly consistent despite the fact that the driver has frequently transitioned in and out of the automated control regardless that the speed was either controlled by the driver or by the automated system.

## **5.2 Precision Docking Demonstration at Washington DC**

Figures 5.2.1 to 5.2.2 show 9 consecutive precision docking demonstration runs for the C2 40-ft bus at the Washington DC Demo test track. The precision docking system was set to be transitioned to automated control automatically for all 9 runs. We select this set of data to highlight the consistent performance when steering, brake and throttle are all under automated control. The driver would manually drive the bus to around the beginning of the magnetic track. Once the precision docking system recognized the magnets under the pavement, the system would first display “ready” (green LED) to the driver, and the automated control system would automatically engaged after about 1.6 seconds. During these runs, the driver simply drove to the test track without specifically lining up with the track, and the bus would transition to precision docking within 1.6 second after the bus recognize the magnetic markers.

Figure 5.2.1 illustrates the lateral positions, steering angle, and speeds with respect to the marker numbers. Each marker number represents one magnet at 1 meter apart. Again,

these plots show convincingly that the tracking repeatability was even higher than that of the RFS testing. Furthermore, the speed and the stop location repeatability also improved significantly than those from manual speed control.

Figure 5.2.2 shows the blow-up plot of Figure 5.2.1 around the S-curve docking station. The blow-up plots clearly show that the bus has never touch the station, and the maximum error after bus is approaching the station is basically within 1.5 centimeter peak-to-peak for front and 1 centimeter peak-to-peak for rear. The docking accuracy is also about 1.5 centimeter peak-to-peak for all runs.

### **5.3 Precision Docking Testing at San Diego**

Figures 5.3.1 to 5.3.3 show 17 consecutive precision docking test runs for the C2 40-ft bus at the South Control Yard test track in San Diego. While Figure 5.3.4 to 5.3.6 plot 14 consecutive runs for the C1 40-ft bus at the same test track. The controllers employed by these two buses were identical. No verification was done to verify whether the two buses were identical in their dynamic characteristics. As described before, the test track in the SCY has two docking stations connected by the magnetic markers: first an in-line station and then a S-curve station. For most of the runs, fully automated control with automatic transition from manual to automatic was conducted. The driver drove toward the magnet track, the bus then transitioned to fully automated controls, and stopped at the first docking in-line docking station. When all the passengers were either got in or got out of the bus, the driver pushed the “auto” button and the bus resumed automated control and stopped again automatically at the second S-curve docking station. In each set of the test runs, several runs were conducted differently to demonstrate the capabilities of the system. These non-normal runs involved stop and go, switching off speed control by stepping on brake, manually stopping at the station, and manually driving off the station. Observing the speed plots in Figures 5.3.1 to 5.3.6 can easily identify these runs.

Figure 5.3.1 and 5.3.4 illustrate the lateral positions, steering angle, and speeds with respect to the marker numbers for Bus C2 and C1, respectively. The two buses exhibited similar performance characteristics and accuracy. The two stations were also identified on the lateral position plot in figure. It is worthwhile noticed that the buses automatically left the bus station and kept away from the platform until the rear of the bus cleared away from the in-line bus station for safety. This can also be observed on the blow-up plots for the first in-line docking station as in Figures 5.3.2 and 5.3.5.

Similarly, Figure 5.3.3 and 5.3.6 show the blow-up plot of Figure 5.3.1 and 5.3.4 around the S-curve docking station. Again, the blow-up plots clearly show that the bus has never touch the station, and the maximum error after bus is approaching the station is basically within 1.5 centimeter peak-to-peak for front and 1 centimeter peak-to-peak for rear. The docking accuracy is also about 1.5 centimeter peak-to-peak for all runs.

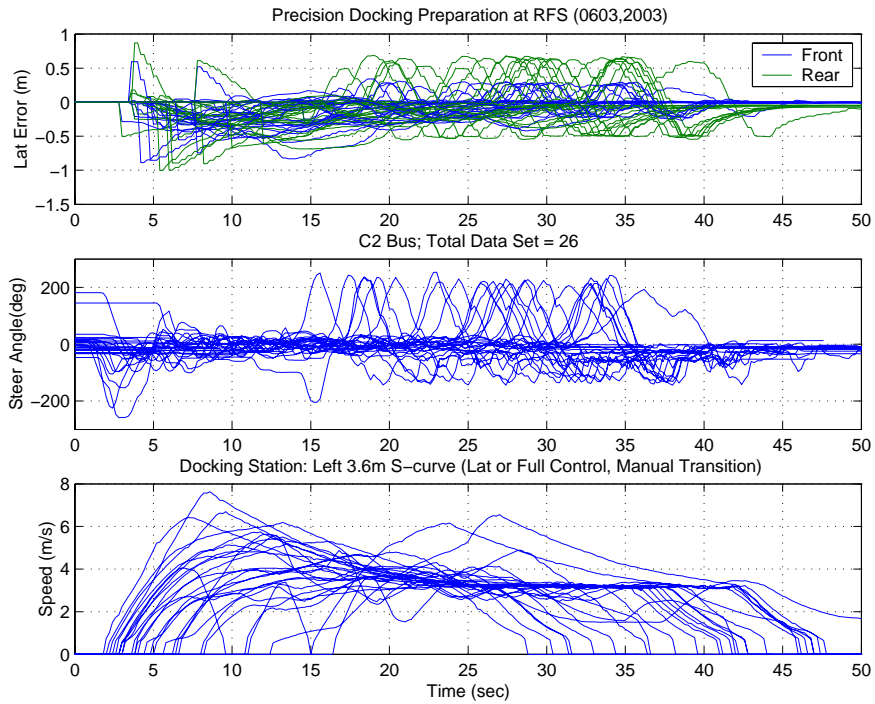


Figure 5.1.1 Precision Docking Preparation at RFS (Time based plot)  
26 consecutive runs; lateral control only and Fully automated, C2 40 ft bus

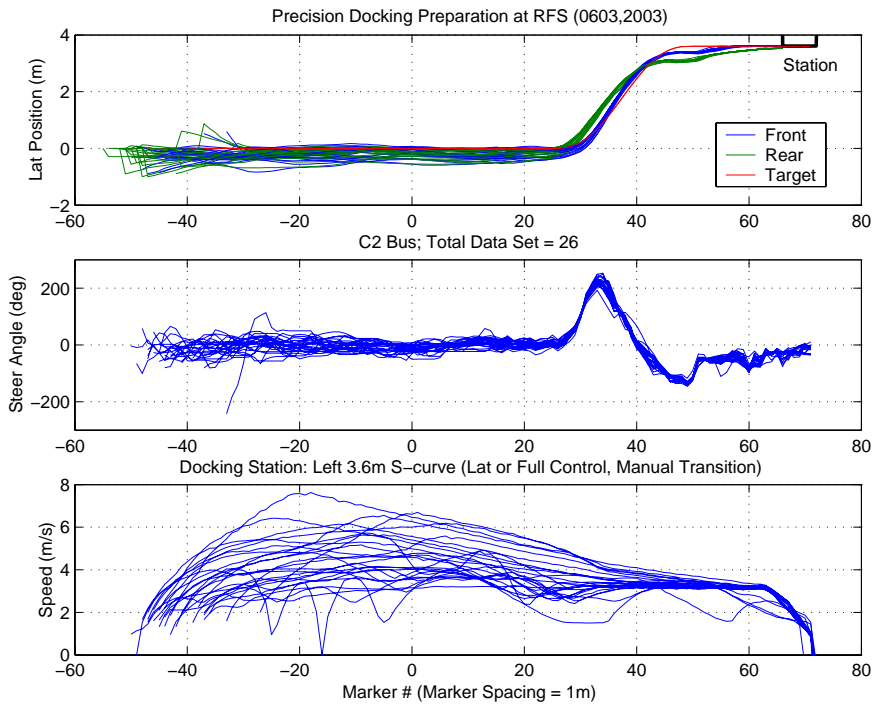


Figure 5.1.2 Precision Docking Preparation at RFS (Marker based plot)  
26 consecutive runs; lateral control only and Fully automated, C2 40 ft bus

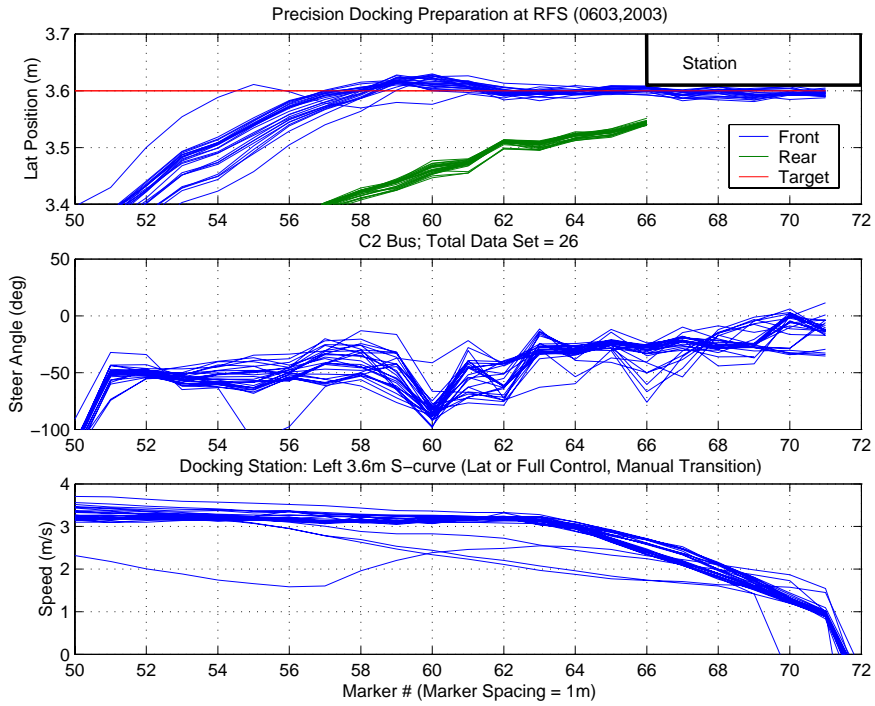


Figure 5.1.3 Precision Docking Preparation at RFS (Marker based plot at Station)  
26 consecutive runs; lateral control only and Fully automated, C2 40 ft bus

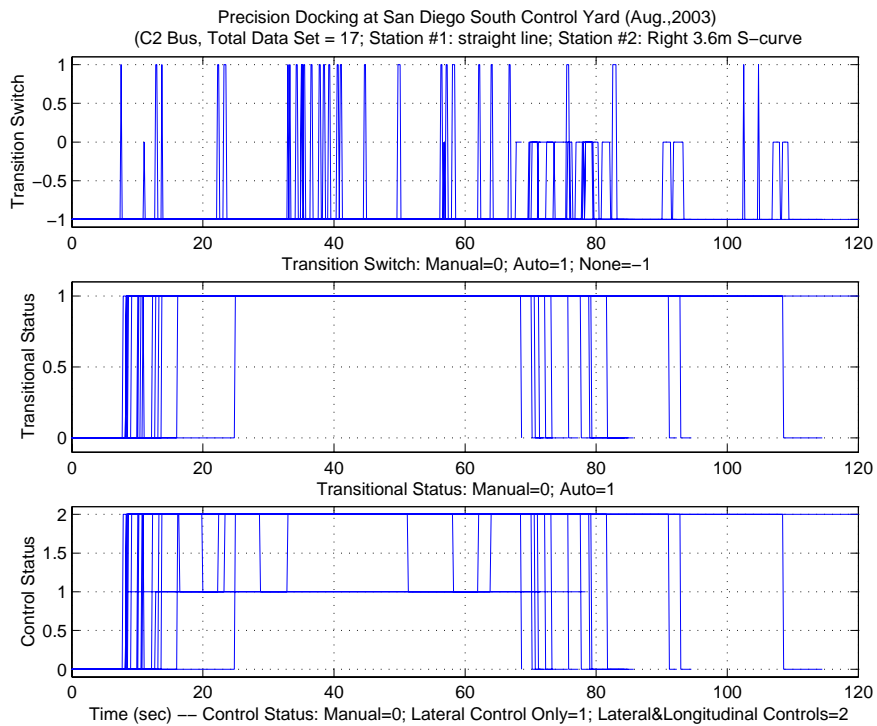


Figure 5.1.4 Precision Docking Preparation at RFS (Time based plot)  
26 consecutive runs; lateral control only and Fully automated, C2 40 ft bus

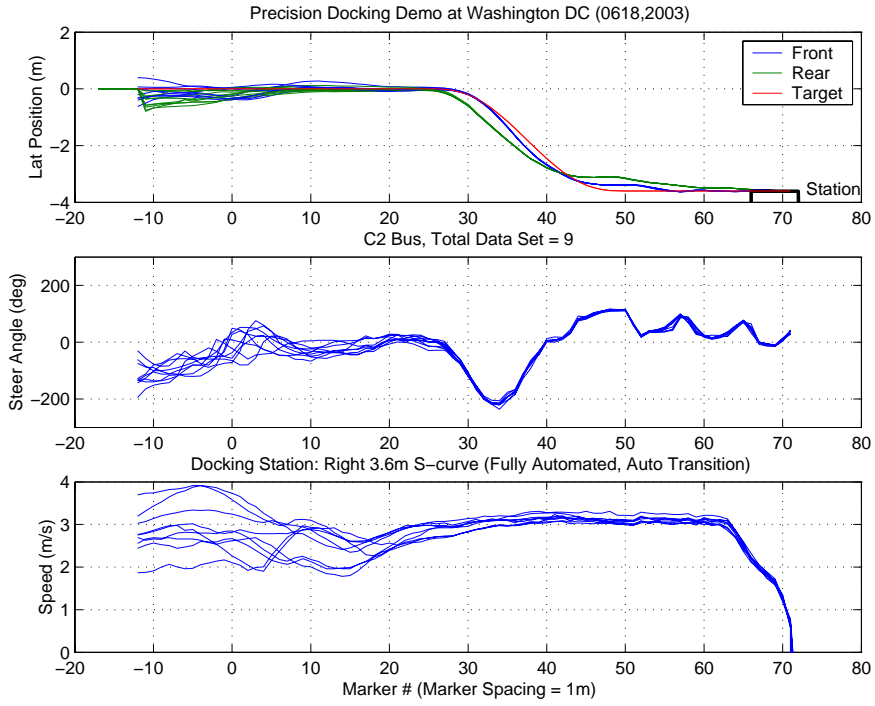


Figure 5.2.1 Precision Docking Demo at DC (Marker based plot) 9 consecutive runs. Fully automated w Automatic transition, C2 40 ft bus

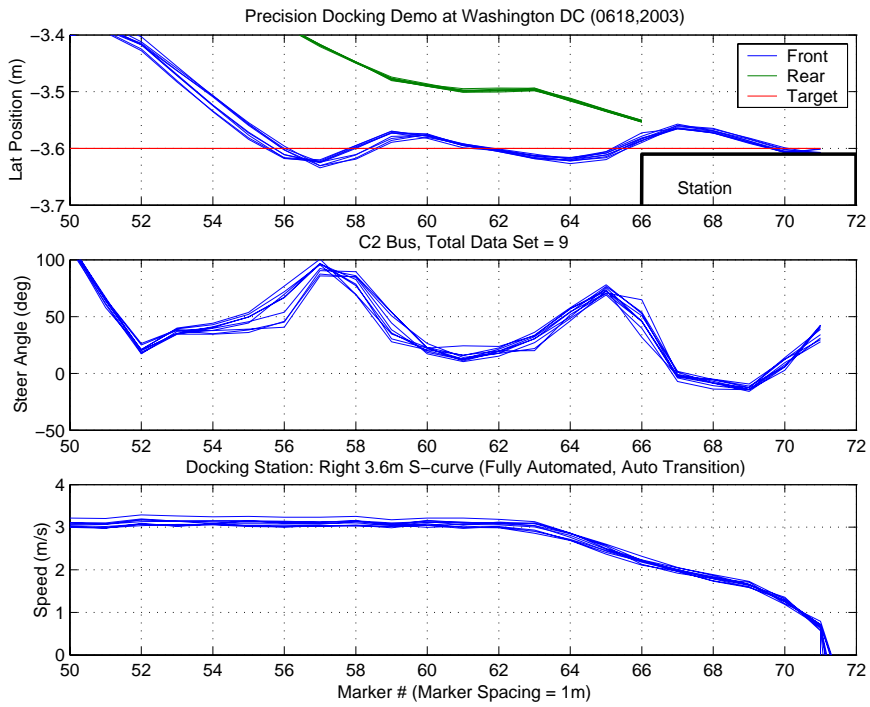


Figure 5.2.2 Precision Docking Demo at DC (Marker based plot) 9 consecutive runs. Fully automated w Automatic transition, C2 40 ft bus



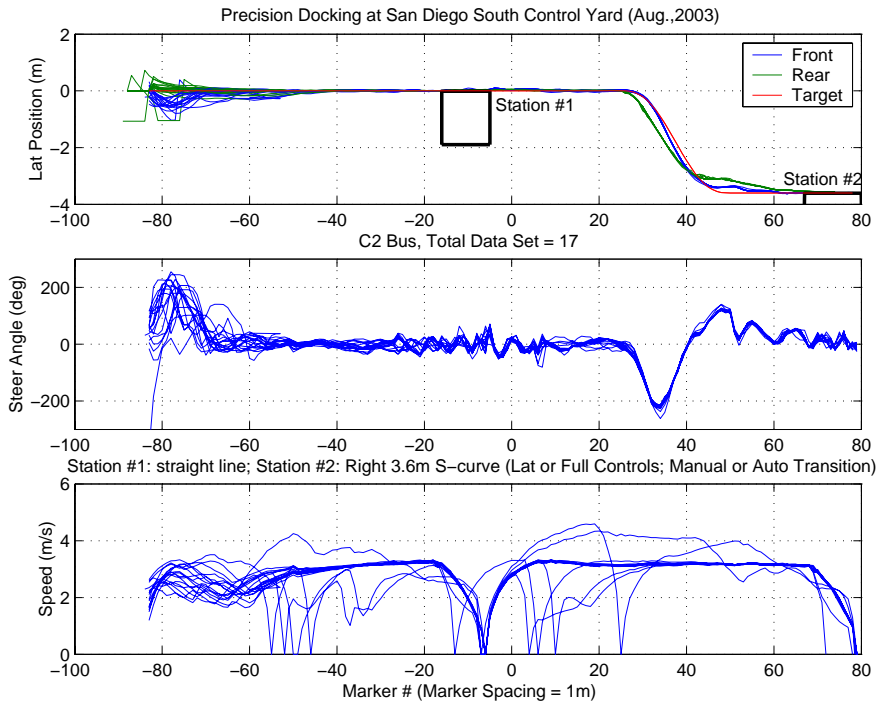


Figure 5.3.1 Precision Docking Testing at SCY (Marker based plot) 17 consecutive runs; Fully/Lateral control w Manual/Automatic transition, C2 40 ft bus

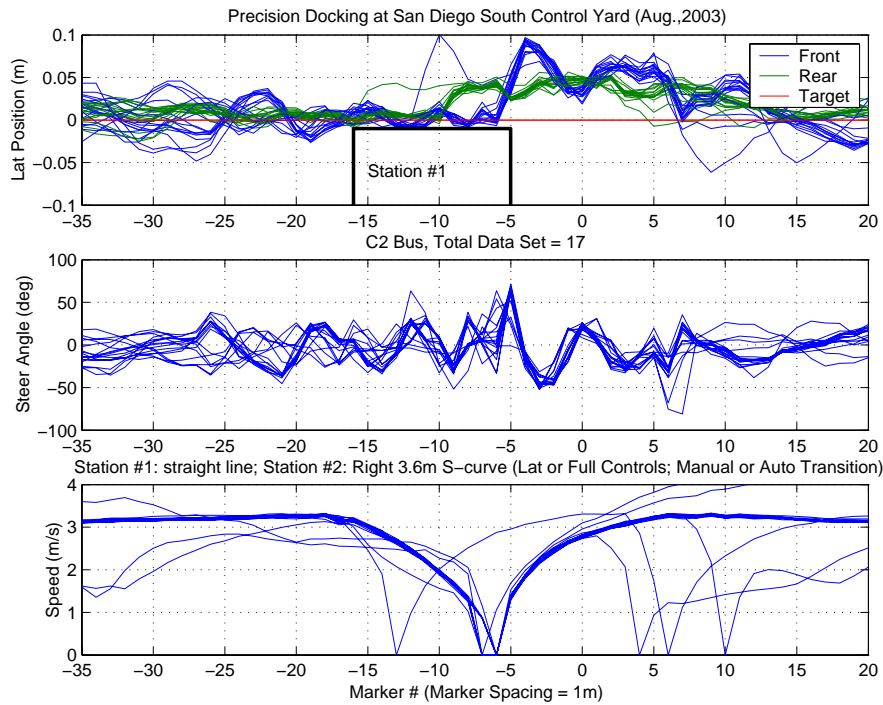


Figure 5.3.2 Precision Docking Testing at SCY (Marker based plot at Station #1) 17 consecutive runs; Fully/Lateral control w Manual/Automatic transition, C2 40 ft bus

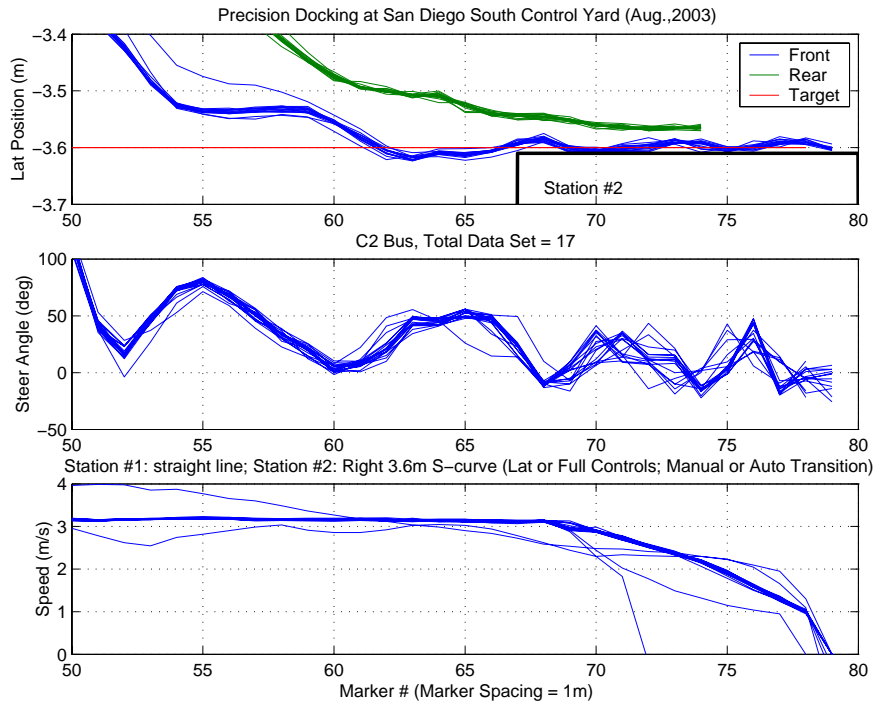


Figure 5.3.3 Precision Docking Testing at SCY (Marker based plot at Station #2)  
17 consecutive runs; Fully/Lateral control w Manual/Automatic transition, C2 40 ft bus

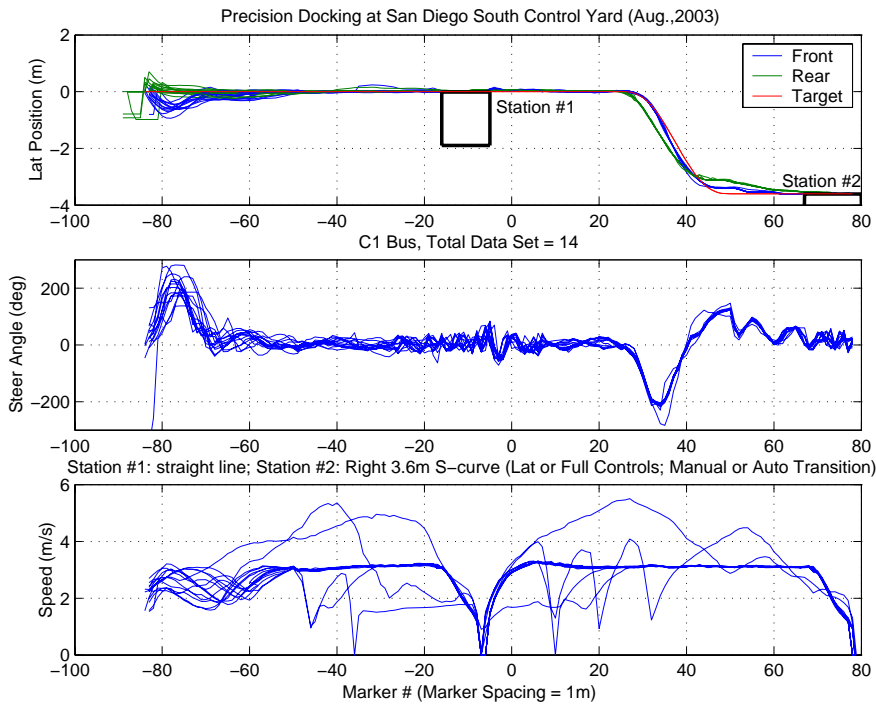


Figure 5.3.4 Precision Docking Testing at SCY (Marker based plot)  
14 consecutive runs; Fully/Lateral control w Manual/Automatic transition, C1 40 ft bus

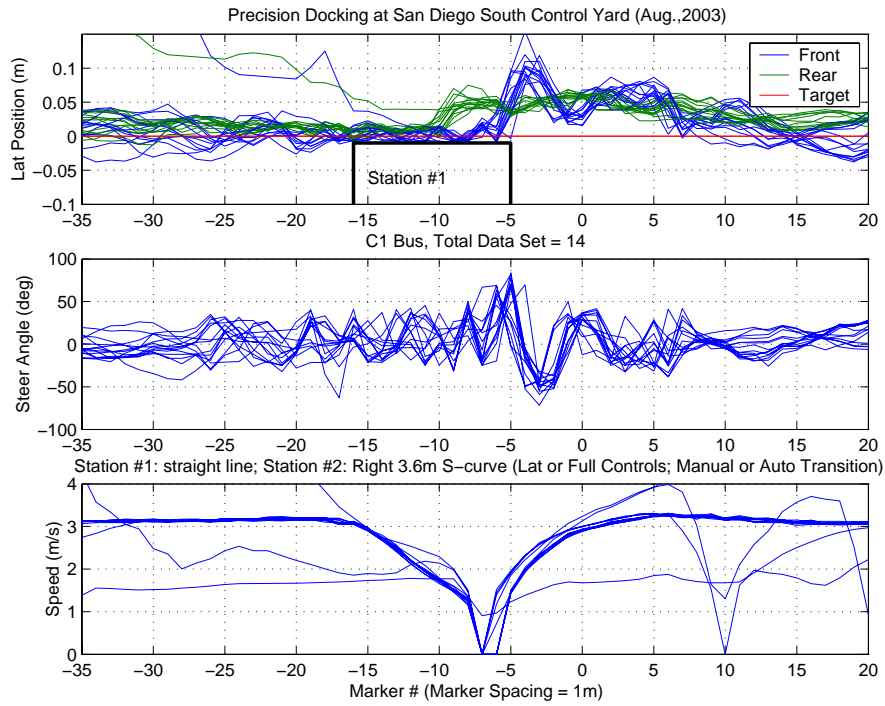


Figure 5.3.5 Precision Docking Testing at SCY (Marker based plot Station #1)  
14 consecutive runs; Fully/Lateral control w Manual/Automatic transition, C1 40 ft bus

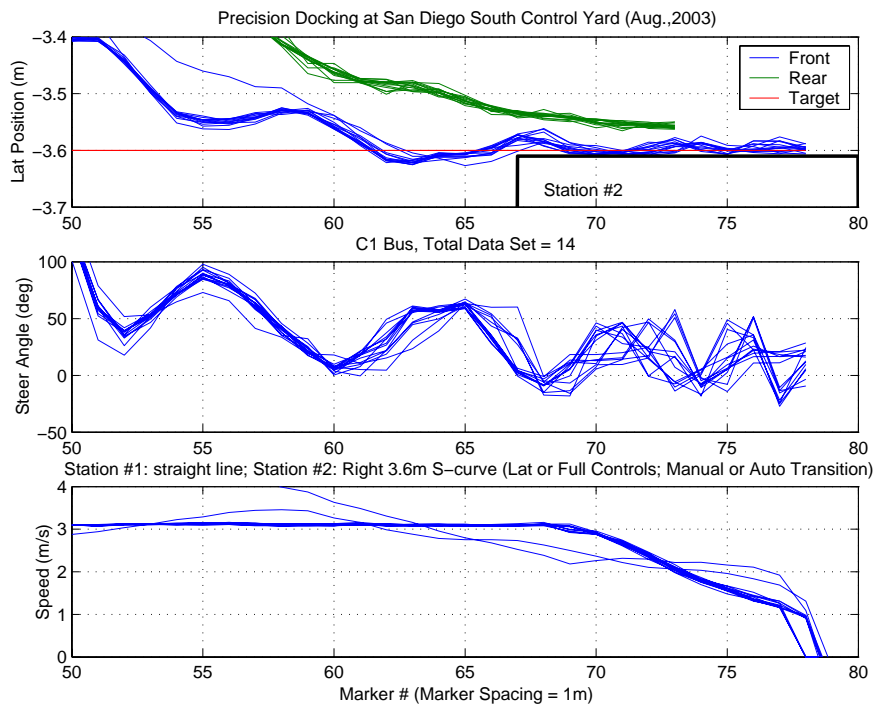


Figure 5.3.6 Precision Docking Testing at SCY (Marker based plot Station #2)  
14 consecutive runs; Fully/Lateral control w Manual/Automatic transition, C1 40 ft bus